nature chemical biology

ARTICLES

https://doi.org/10.1038/s41589-018-0086-4

Rab11 activity and PtdIns(3)*P* turnover removes recycling cargo from endosomes

Carlo Cosimo Campa[1,4*], Jean Piero Margaria[1,4], Abhishek Derle[1,5], Marco Del Giudice[2,3,5], Maria Chiara De Santis[1], Luca Gozzelino[1], Francesca Copperi[1], Carla Bosia[2,3] and Emilio Hirsch[1*]

Directional transport of recycling cargo from early endosomes (EE) to the endocytic recycling compartment (ERC) relies on phosphatidylinositol 3-phosphate (PtdIns(3)*P*) hydrolysis and activation of the small GTPase Rab11. However, how these events are coordinated is yet unclear. By using a novel genetically-encoded FRET biosensor for Rab11, we report that generation of endosomal PtdIns(3)*P* by the clathrin-binding phosphoinositide 3-kinase class 2 alpha (PI3K-C2α) controls the activation of Rab11. Active Rab11, in turn, prompts the recruitment of the phosphatidylinositol 3-phosphatase myotubularin 1 (MTM1), eventually enabling the release of recycling cargo from the EE and its delivery toward the ERC. Our findings thus define that delivery of recycling cargo toward the ERC requires spatial and sequential coupling of Rab11 activity with PtdIns(3)*P* turnover.

Intracellular trafficking of endocytosed molecules ensures the delivery of plasma-membrane components and receptor-associated ligands to several cellular compartments. After internalization, such molecules can be either degraded or re-used by returning to the plasma membrane[1]. This recycling pathway restores the composition of plasma membrane and is mediated by vesicular carriers that transfer endocytosed material from peripherally located early endosomes (PE) to the endocytic recycling compartment (ERC), a juxtanuclear tubulovesicular compartment[2–4]. To be effective, this transport route requires regulated recruitment of molecular motors, membrane tethers, and lipid kinases and phosphatases in time and space[5–12]. Such engagement is partly accomplished by key determinants of functional identity of organelles including PtdIns(3)P and the small GTPase Rab11 (refs [9,13–16]).

PtdIns(3)*P* is the major phosphoinositide residing on early endosomes, where it serves as a membrane recognition site for the recruitment of proteins, thereby mediating endosomal fusion and maturation[17,18]. PtdIns(3)P homeostasis is controlled by the coordinated action of lipid kinases and phosphatases. In particular, whereas phosphorylation of PtdIns to PtdIns(3)*P* requires members of the class II and class III phosphatidylinositol 3-kinase (PI3K) enzymes[10,19–21], termination of PtdIns(3)*P* signaling relies on myotubularins (MTMs), lipid phosphatases that convert PtdIns(3)*P* to (PtdIns)[22–25]. Although endosome maturation and recycling of endocytosed cargos requires control of PtdIns(3)*P* levels by the action of lipid kinases and phosphatases[8,22,26], the mechanism responsible for the regulated recruitment of these lipid metabolizing enzymes on endosomes remains largely unknown.

Extensive investigations demonstrated that members of the Rab protein family are coordinators of membrane domain formation and vesicle trafficking dynamics controlling the recruitment of endocytic regulators such as lipid kinases or phosphatases[27]. In particular, trafficking of endocytosed cargos toward the ERC is mediated by Rab11, a small GTPase that is enriched on ERC membranes and activated by signaling downstream of PI3K-C2α-derived PtdIns(3)*P* pool[9,10,20,28]. In its active GTP-bound form, Rab11 mediates recycling and sorting of endocytosed membrane components through the ERC[12–14,29]. However, whether the changes in Rab11 activity might determine the efficiency of membrane trafficking by controlling the phosphoinositide composition of endosomes is still unclear.

To monitor changes in Rab11 activity in living cells, we developed a genetically encoded FRET biosensor of active Rab11 named activation sensor Rab11 (AS-Rab11). Using this biosensor, we demonstrated that the increase in Rab11 activity on PtdIns(3)P^+ peripheral endosomes is important for controlling the release of recycling cargoes via a circuit involving a sequential clathrin/PI3K-C2α-mediated PtdIns(3)*P* burst and subsequent Rab11/MTM1-dependent PtdIns(3)*P* hydrolysis.

Results

Development of a Rab11 FRET biosensor. The activation cycle of Rab11 is essential to mediate the delivery of internalized plasma membrane components from the PE to the ERC[1,30]. To monitor the spatial and temporal regulation of Rab11 nucleotide exchange in living cells, the genetically encoded fluorescence resonance energy transfer (FRET)-based probe AS-Rab11 was developed (Fig. 1a; Supplementary Fig. 1a,b). The probe includes the C-terminal region of FIP3-binding active Rab11[31], a circular permuted version of a modified monomeric yellow fluorescent protein (mcpVenus), a proteinase K-sensitive linker, a monomeric cyan fluorescent protein (mECFP), and human Rab11a (Fig. 1a). In this probe design, an increase in GTP loading of Rab11 promotes the binding of the C-terminal region of FIP3 to Rab11a, thus modifying the orientation of the two fluorophores and thereby increasing FRET, which is represented by the 525 nm/475 nm (FRET/CFP) emission ratio[32,33] (Fig. 1a). The positioning of Rab11 at the C-terminal end of AS-Rab11 enables correct functioning of the Rab11 C-terminal sequences required for membrane insertion (Fig. 1a).

To validate the efficiency of the biosensor energy transfer in the presence of either GDP or GTP, we monitored the fluorescence emission profiles of AS-Rab11 using a fluorometric assay

[1]Department of Molecular Biotechnology and Health Sciences. Molecular Biotechnology Center, University of Turin, Torino, Italy. [2]Department of Applied Science and Technology, Politecnico di Torino, Torino, Italy. [3]Italian Institute for Genomic Medicine, Torino, Italy. [4]These authors contributed equally: Carlo Cosimo Campa, Jean Piero Margaria. [5]These authors jointly supervised this work: Abhiskek Derle, Marco Del Giudice. *e-mail: carlocosimo.campa@unito.it; emilio.hirsch@unito.it

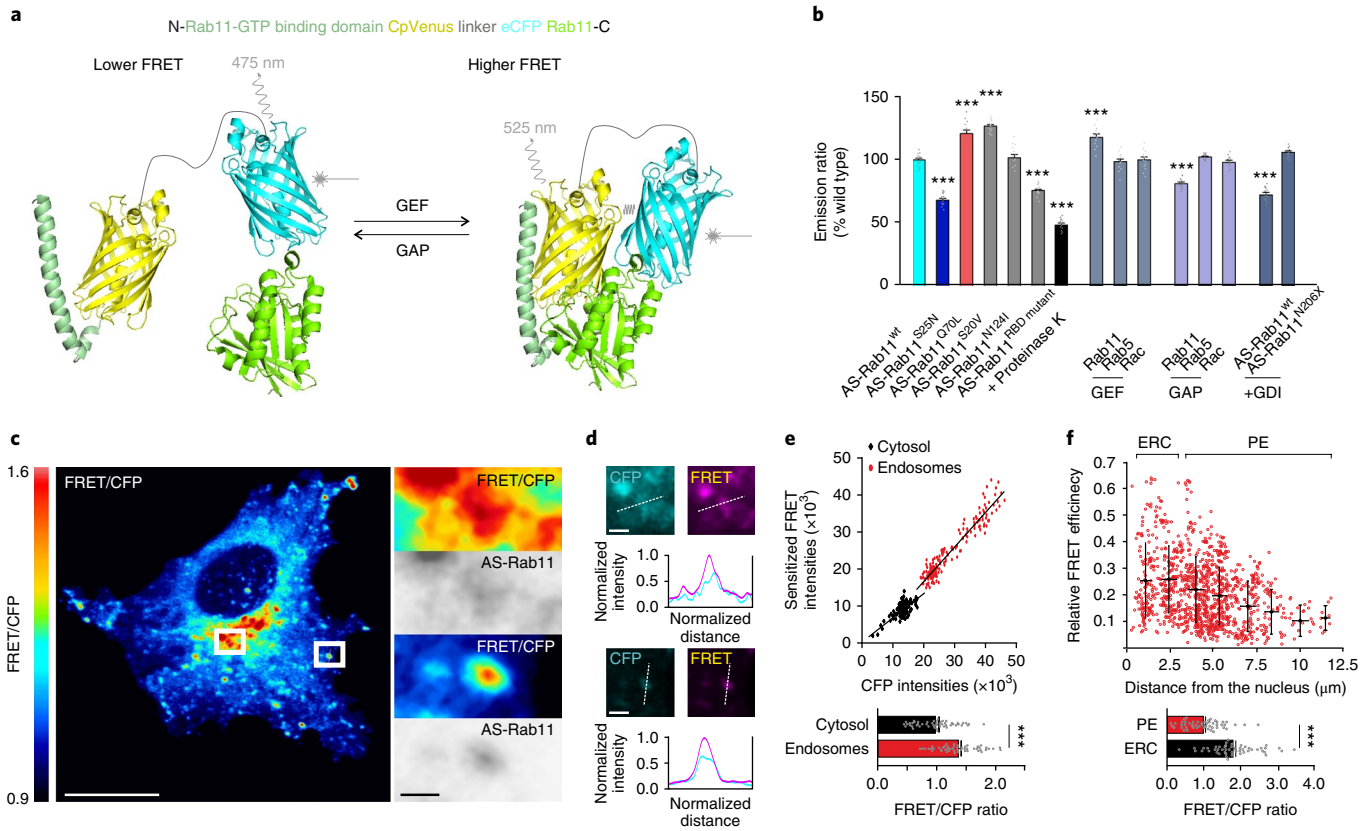

Fig. 1 | The FRET biosensor AS-Rab11 specifically measures Rab11 nucleotide binding status. a, Tridimensional representation of the genetically encoded fluorescence energy transfer (FRET) probe AS-Rab11 (activation sensor Rab11) in its inactive (bound to GDP, left) or active conformation (bound to GTP, right). Yellow and light blue β-barrels represent yellow- and cyan-emitting mutants of fluorescent proteins, respectively. Sea-green α-helix, black line, and green β-barrels structures indicate the Rab11-GTP-binding domain (C-terminal region of FIP3), the proteinase K sensitive linker domain and the Rab11a protein, respectively. In this probe design, an increase of Rab11 GTP loading promotes the binding of the C-terminal region of FIP3 to Rab11a, modifying the relative orientation of the two fluorophores and thereby increasing FRET signal. **b**, Quantifications of FRET efficiency of AS-Rab11^{wt}, AS-Rab11 mutant forms, and proteinase-K-treated AS-Rab11^{wt}, as well as AS-Rab11^{wt} co-expressed with the indicated GEFs and their target GTPases (SH3BP5, RABEX-5, and TIAM1, respectively), AS-Rab11^{wt} co-expressed with the indicated GAPs and their target GTPases (TBC1D9B, RN-3, and ARHGAP15, respectively), and AS-Rab11^{wt} or AS-Rab11^{N206X} co-expressed with RabGDI ($n = 12$ independent experiments; data represent mean ± s.e.m.; $^{***}P < 0.005$; one-way ANOVA). **c**, Representative FRET/CFP ratio images of the AS-Rab11 biosensor in COS-7 cells (pseudocolor images represent FRET/CFP ratio intensity values). The upper and lower limits of the FRET/CFP ratio are shown on the left side bar. Magnification of FRET/CFP ratio images and AS-Rab11 localization in juxtanuclear (upper) and peripheral endocytic structures (lower). Right panel, pseudocolor images represent FRET/CFP ratio intensity values; grayscale image indicates emission of mcpVenus (AS-Rab11) after its direct excitation). Scale bars, 10 μm. **d**, Representative line intensity profile of FRET sensitized (magenta) and CFP (cyan) signal detected in juxtanuclear (top) and peripheral (bottom) endocytic structures. The magenta and cyan images represent FRET sensitized and CFP signals, respectively. Scale bars, 1 μm. **e**, Top, scatter plot of sensitized FRET intensities as a function of CFP intensities in AS-Rab11-expressing cells (black and red dots represent the sensitized FRET and CFP intensity of cytosolic and membrane-bound structures, respectively; regression line is in black; $n = 4$ independent experiments). Bottom, quantification of the FRET/CFP ratio between cytosolic and endocytic structures labeled by AS-Rab11 ($n = 50$ independent experiments; data represent mean ± s.e.m.; $^{***}P < 0.005$; two-tailed unpaired t-test). **f**, Top, scatter plot of relative FRET efficiency as a function of distance from the nucleus for endocytic structures labeled by AS-Rab11 ($n = 4$ independent experiments; black line represents mean ± s.e.m.). Bottom, quantification of the FRET/CFP ratio between juxtanuclear (ERC, 0 to 3 μm from nucleus) and peripheral (PE, 3 to 12 μm from the nucleus) endocytic structures labeled by AS-Rab11 ($n = 50$ independent experiments; data represent mean ± s.e.m.; $^{***}P < 0.005$; t-test).

(see Methods). In comparison to the wild-type form, constitutively active mutant versions of Rab11 lacking GTPase activity (AS-Rab11^{Q70L} and AS-Rab11^{S20V}) showed decreased fluorescence emission intensity at 475 nm and a concomitant increase at 525 nm (Fig. 1b; Supplementary Fig. 1c red line). Consequently, the FRET/CFP ratio of AS-Rab11^{Q70L} and AS-Rab11^{S20V} were found to be significantly higher than the wild-type and the nucleotide-free (AS-Rab11^{N124I}) forms (Fig. 1b; Supplementary Fig. 1c). In contrast, a dominant negative version of this biosensor (AS-Rab11^{S25N}; Supplementary Fig. 1c, blue line) displayed a 475 nm emission and an associated 525 nm emission that were higher and lower than the control, respectively (Fig. 1b; Supplementary Fig. 1c,d, cyan line). A similar observation was made after treatment of wild-type AS-Rab11 (AS-Rab11^{wt}) with proteinase-K (Supplementary Fig. 1c, black line), which induced the cleavage of the amino acidic linker connecting the two fluorophores required to promote the energy transfer. Consequently, both AS-Rab11^{S25N} and proteinase-K-treated AS-Rab11^{wt} showed a decreased FRET emission ratio (Fig. 1b; Supplementary Fig. 1c, blue and black lines), similarly to a Rab11-GTP-binding mutant (AS-Rab11$^{RBD\ mutant}$) (Fig. 1b). In line with these results, increased FRET emission ratio and Rab11-GTP content were detected after co-expression of AS-Rab11^{wt} with SH3BP5, a Rab11-GEF[34] (Fig. 1b; Supplementary Fig. 1e). On the contrary, co-expression of TBC1D9B, a Rab11-GAP[35], decreased FRET emission ratio and

Rab11-GTP content in cells (Fig. 1b; Supplementary Fig. 1e). A similar emission was obtained by co-expression of RabGDI, a Rab11 dissociation inhibitor[36], which was reverted by the use of a guanosine nucleotide dissociation inhibitor (GDI)-insensitive biosensor mutant (AS-Rab11^{N206X}; Fig. 1b). This regulation was found to be specific, as co-expression of AS-Rab11^{wt} with either Rac1 or Rab5 GEFs (guanine nucleotide exchange factors) and GAPs (GTPase-activating proteins) had no effect on biosensor response (Fig. 1b). Next, AS-Rab11 binding to guanine nucleotides was assessed by thin-layer chromatography. Equal amounts of GDP and GTP associated with the wild-type biosensor form, whereas either GTP or GDP bound the constitutively active (Q70L) or the dominant negative (S25N) biosensor forms, respectively (Supplementary Fig. 1f). At the same time, AS-Rab11 was able to bind and replace GDP with GTP, similarly to Rab11 (Supplementary Fig. 1g). The biosensor was found to interact with recombinant FLAG-RabGDI, FLAG-SH3BP5, and FLAG-TBC1D9B (Supplementary Fig. 2a–c). Whereas AS-Rab11$^{RBD\ mutant}$ interacted with endogenous FIP2 and FIP4, AS-Rab11^{WT} did not, indicating that the probe in its active conformation is not able to compete for endogenous targets (Supplementary Fig. 2d). Finally, As-Rab11 localized with markers of early and recycling endosomes but was absent from cis-Golgi and late endosome structures (Supplementary Fig. 3a–e), thus showing a pattern consistent with the functions of unmodified, endogenous Rab11.

Increased FRET emission ratio was detected both on tubulovesicular structures situated in the proximity of the nucleus and on small membrane-bound organelles positioned at the cell periphery (Fig. 1c,d). To exclude the possibility that such high FRET efficiency was caused by random probe accumulation, we generated a correlation plot of the sensitized FRET (i.e., the measure of FRET efficiency corrected for excitation and emission cross-talk) versus the CFP intensities. Sensitized FRET was higher in endosomes than in cytosol (Fig. 1e), as indicated by the two different slopes of the regression line that correlate to the sensitized FRET and the CFP intensities measured in endosomes and cytosol, respectively. Moreover, to assess the spatial distribution of active Rab11 in cells, we measured the FRET/CFP ratio of structures as a function of distance from the nucleus, and the FRET emission ratio appeared to be significantly higher on the ERC than on the PE (Fig. 1f).

Overall, these results demonstrate that this biosensor can monitor the nucleotide-binding status of Rab11 and that active Rab11 is spatially restricted in both peripheral and juxtanuclear endosomal structures.

Activated-Rab11 labels PtdIns(3)*P*$^+$ endosomes. To examine the subcellular distribution and the identity of membrane-bound structures displaying active Rab11, AS-Rab11-expressing cells were analyzed by confocal microscopy after the internalization of fluorescent transferrin (Tf-647), an early-recycling endosome marker[16]. In line with previous studies[13,14], perinuclear accumulation of active Rab11 (Fig. 2a, left panel, pseudocolor map) and Tf-647 (Fig. 2a, left panel, gray scale) was observed. In addition, enlargement of the periplasmalemmal-region showed overlap between the highest FRET signal (Fig. 2a, right panel, red line) and Tf-647 (Fig. 2a, right panel, black line). Accordingly, a two-dimensional representation of pixel intensities (Fig. 2a, right panel, line intensity profile) along a line starting from the nucleus and reaching the plasma membrane (Fig. 2a, left panel, white line) showed almost perfect overlap between FRET ratio (Fig. 2a, right panel, red line) and Tf-647 (Fig. 2a, right panel, black line) signals in both the perinuclear and peripheral region. In further agreement, analysis of colocalization, as determined by Pearson's coefficient, showed high correlation between FRET ratio and Tf-647 positivity in both the ERC and PE (Fig. 2a, right panel), indicating that active Rab11 is equally distributed in perinuclear and peripheral Tf-positive compartments.

To gain insight into the localization of active Rab11, early and recycling endosome-specific markers were similarly studied by analyzing a red fluorescent tagged version of either Rab4, Rab5, or the PtdIns(3)*P* probe mCherry-FYVE2X. Identical distribution and strong colocalization were observed by fine mapping of active-Rab11 and mRFP-Rab4-positive structures in pseudocolor and grayscale, respectively (Fig. 2b). Conversely, endosomal membranes labeled by mRFP-Rab5 colocalized with active Rab11 at the cell periphery, but not at the perinuclear recycling compartment (Fig. 2c). Similarly, active-Rab11 strongly colocalized with the early endosome marker PtdIns(3)*P* on peripheral but not on perinuclear membrane-bound structures, as detected with the mCherry-FYVE2X probe (Fig. 2d). These results indicate that PEs in which active Rab11 colocalized with PtdIns(3)*P* correspond to early endosomes.

Exit from endosome relies on Rab11 and PtdIns(3)*P*. To examine the relationship between Rab11, PtdIns(3)*P* and recycling cargo in peripheral endosomes, we monitored the localization of Rab11 and transferrin receptor (TfR) on PtdIns(3)*P*-positive structures during the continuous uptake of Tf. Confocal microscopy analysis revealed a frequent growth of tubular Rab11$^+$/mCherry-TfR$^+$ structures from PEs (Fig. 3a). Furthermore, Tf uptake increased Rab11 activity (Supplementary Fig. 4a,b), and expression of a Rab11 dominant negative form inhibited Tf recycling and promoted its accumulation (Supplementary Fig. 4c–e), thus indicating that removal of recycling cargo from endosomes requires Rab11 activation. In agreement, increased FRET/CFP signal on the nascent vesicle began 5 s before fission, concomitantly with a PtdIns(3)*P* burst, and reached maximal signal at the time of fission (Fig. 3b,c; Supplementary Fig. 4f–h). Such activation kinetics did not rely on biosensor abundance, as both temporal assessment and titration of AS-Rab11 levels on endosomes showed robust and coherent biosensor responses at various probe expression levels (Fig. 3c, gray line; Supplementary Fig. 4i). Unexpectedly, on the nascent recycling structure, Rab11 activation was initially preceded by the increase of PtdIns(3)*P* levels but later followed by a decrease in PtdIns(3)*P*, starting at the time of fission (Fig. 3b,c; Supplementary Fig. 4f–h). These results show that, on peripheral endosomes, PtdIns(3)*P* peaks concomitantly with Rab11 activation and declines with the fission of recycling cargo-containing vesicles.

To gain insight into this process, COS-7 cells expressing perinuclear localized AS-Rab11 were bleached to avoid contaminating signals from the ERC region, and movement of active Rab11$^+$ vesicles was analyzed after addition of Tf (Fig. 3d). Rab11$^+$ vesicles followed long-range linear movements and then eventually collapsed into ERC membranes (Fig. 3d), thus indicating that juxtanuclear AS-Rab11-positive structures are derived in part from peripheral endosomes. Accordingly, AS-Rab11-positive endosomal structures accumulated in the perinuclear region during the continuous uptake of Tf and resulted in a steady state after 15 min (Supplementary Fig. 5a–e). By interfering with microtubule polymerization using a treatment with nocodazole, vesicles carrying an active Rab11 failed to appear as a linear series of dots over time (Supplementary Fig. 5f). This indicated that disruption of microtubule-dependent transport abolished long-range movements of AS-Rab11-positive membranes without compromising Tf accumulation (Supplementary Fig. 5f–h). Consistently, displacement of endocytic structures, as well as Rab11 activation, were decreased upon nocodazole treatment (Fig. 3e,f). These data suggested that minus-end-directed microtubule motor transport is required for endocytic structure movement. To test this hypothesis, acute inactivation of retrograde transport using ciliobrevin D, a dynein inhibitor[37], was performed. Ciliobrevin D treatment decreased long-range retrograde motion of active Rab11$^+$ vesicles and had a minor impact on vesicle linear movement and displacement (Fig. 3e,g,h), consistent with multiple Rab11/microtubule-dependent trafficking routes[38]. Finally, both nocodazole and

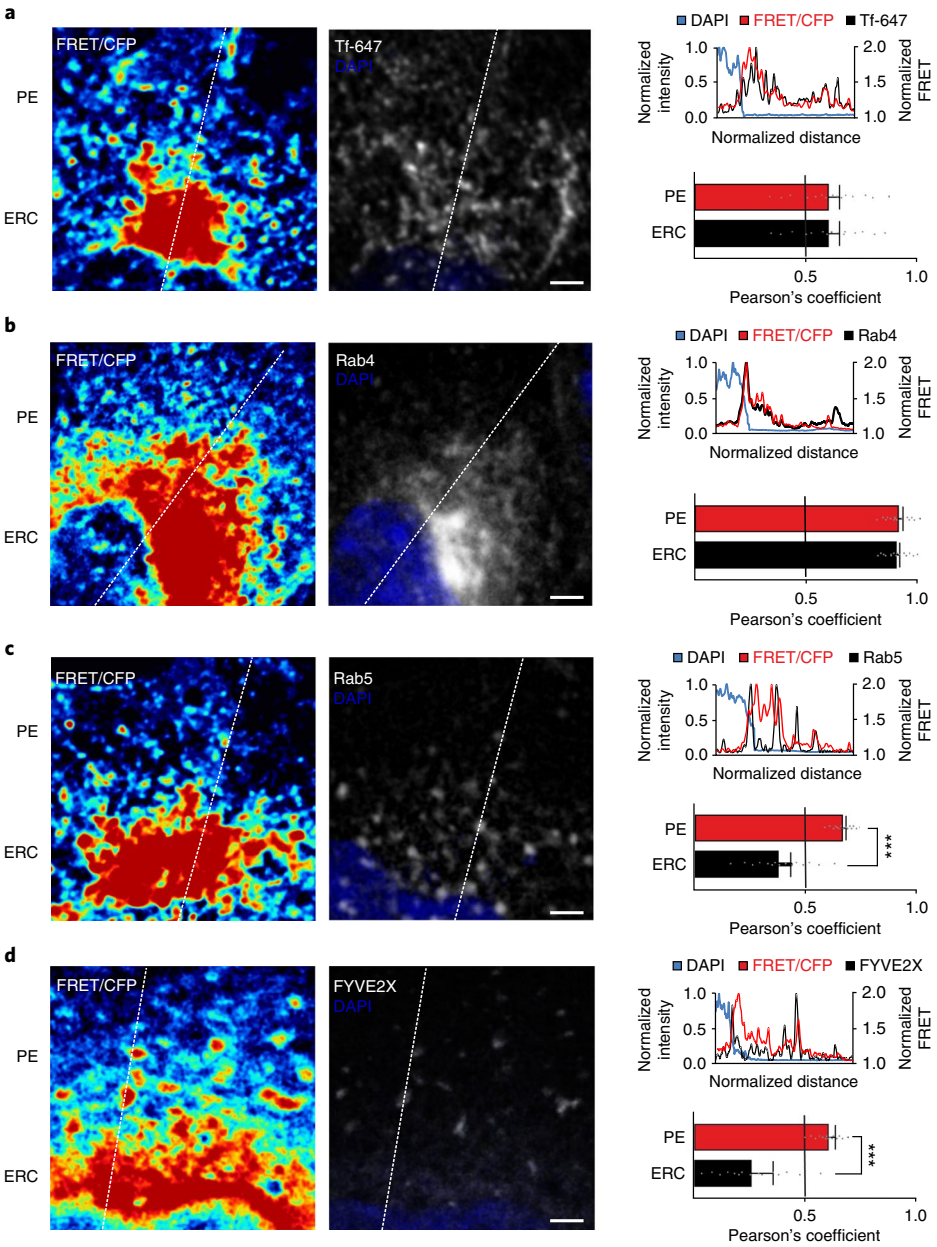

Fig. 2 | Juxtanuclear and peripheral localization of active Rab11 on distinct endosome populations. a, Representative localization of active Rab11 on transferrin-positive endosomes. FRET/CFP ratio images (pseudocolor mode) of the AS-Rab11 biosensor on endosomes labeled by fluorescent transferrin (gray scale). White line defines the region over which the FRET/CFP ratio and fluorescence transferrin signal were measured. Scale bar, 1 µm. Top right, line intensity profile of the FRET/CFP ratio (red), labeled transferrin (black) and nuclei (blue). Bottom right, quantification in juxtanuclear (ERC) and peripheral (PE) endosomes of colocalization percentage (Pearson's correlation coefficient) between FRET/CFP signal and transferrin-labeled endocytic structures ($n = 15$ independent experiments; data represent mean ± s.e.m.; two-tailed, unpaired t-test). **b**, Representative localization of active Rab11 on Rab4-positive endosomes. FRET/CFP ratio images (pseudocolor mode) of AS-Rab11 biosensor on endosomes labeled by mRFP-Rab4 (gray scale). The white line defines the region over which the FRET/CFP ratio and mRFP-Rab4 signal were measured. Scale bar, 1 µm. Top right, Line intensity profile of the FRET/CFP ratio (red), mRFP-Rab4 (black) and nuclei (blue). Bottom right, quantification in juxtanuclear (ERC) and peripheral (PE) endosomes of colocalization percentage (Pearson's correlation coefficient) between FRET/CFP signal and Rab4-labeled endocytic structures ($n = 15$ independent experiments; data represent mean ± s.e.m.; t-test). **c**, Representative localization of active Rab11 on Rab5-positive endosomes. FRET/CFP ratio images (pseudocolor mode) of AS-Rab11 biosensor on endosomes labeled by mCherry-Rab5 (gray scale). White line defines the region over which the FRET/CFP ratio and mCherry-Rab5 signal were measured. Scale bar, 1 µm. Top right, line intensity profile of FRET/CFP ratio (red), mCherry-Rab5 (black) and nuclei (blue). Bottom right, quantification in juxtanuclear (ERC) and peripheral (PE) endosomes of colocalization percentage (Pearson's correlation coefficient) between FRET/CFP signal and Rab5-labeled endocytic structure ($n = 15$ independent experiments; data represent mean ± s.e.m.; $^{***}P < 0.005$; t-test). **d**, Representative localization of active Rab11 on PtdIns(3)P-positive endosomes. FRET/CFP ratio images (pseudocolor mode) of AS-Rab11 biosensor on endosomes labeled by mCherry-FYVE2X (gray scale). White line defines the region over which FRET/CFP ratio and mCherry-FYVE2X signal were measured. Scale bar, 1 µm. Line intensity profile of FRET/CFP ratio (red), mCherry-FYVE2X (black) and nuclei (blue). Quantification in juxtanuclear (ERC) and peripheral (PE) endosomes of colocalization percentage (Pearson's correlation coefficient) between FRET/CFP signal and PtdIns(3)P-labeled endocytic structures ($n = 15$ independent experiments; data represent mean ± s.e.m.; $^{***}P < 0.005$; t-test).

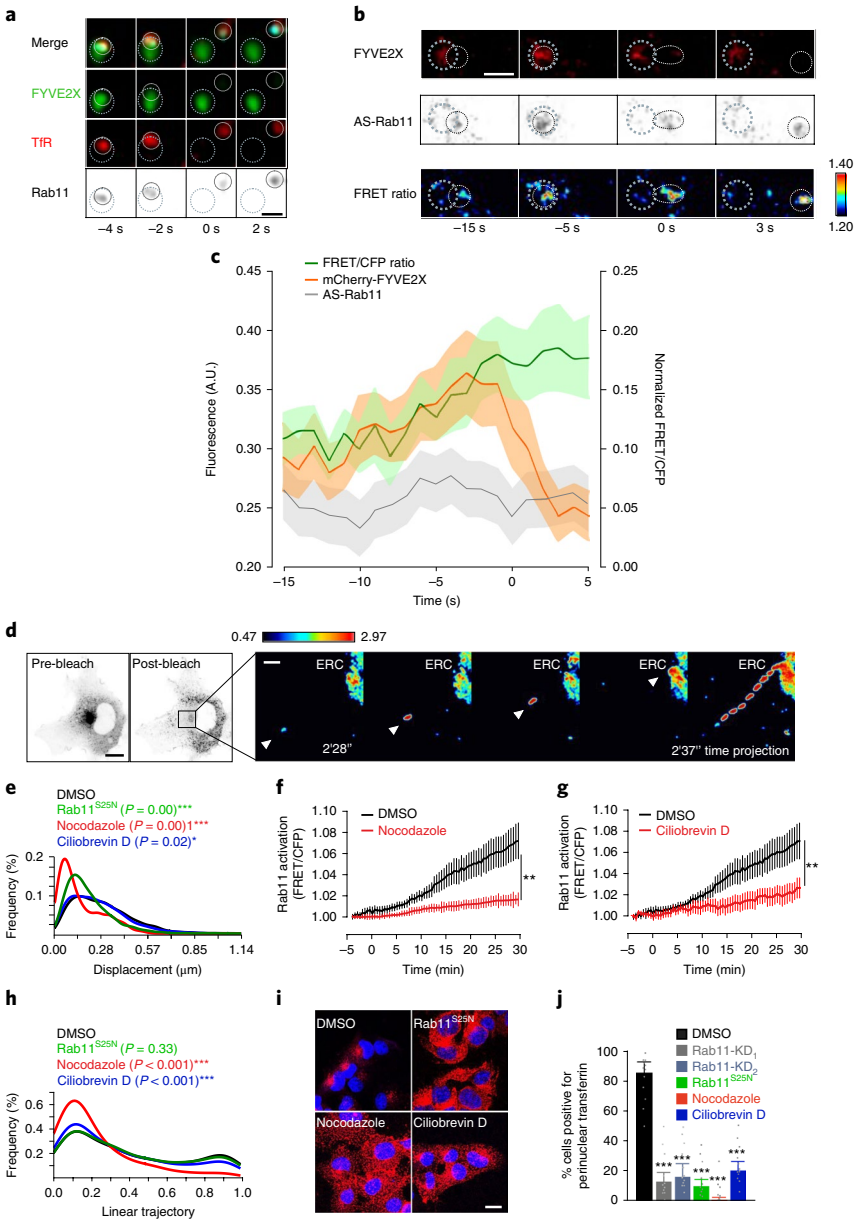

Fig. 3 | Rab11 activation kinetics on PtdIns(3)*P*-positive endosomes. a. Representative time-lapse series of cells co-expressing the mCherry-transferrin receptor (TfR), mECFP-Rab11 and GFP- FYVE2X. White circles represent membrane-bound structures. Scale bar, 1 μm. **b**, Representative time-lapse series of cells co-expressing AS-Rab11 and mCherry-FYVE2X. White circles represent membrane-bound structures. The pseudocolor mode represents the FRET/CFP ratio; gray scale indicates the emission of mcpVenus after its direct excitation. Scale bar, 1 μm. **c**, Quantification of the FRET/CFP ratio (green line), mCherry-FYVE2X fluorescence emission (orange line) and AS-Rab11 mcpVenus emission (gray line) as a function of time in 28 individual vesicle tracks directed toward the ERC. The time point of detachment from early endosomes was recorded and used to shift the time courses so that all 28 detachment events were synchronized at the chosen time point of 0 s. The normalized FYVE2X is shown on the primary *y* axis. The normalized value of FRET/CFP ratio is shown on the secondary *y* axis ($n = 4$ independent experiments). **d**, Representative time-lapse series of long-range transport of an active Rab11 vesicle toward the ERC. Gray scale represents mcpVenus fluorescence emission intensities before and after bleaching (left; scale bar, 5 μm). Magnification shows the juxtanuclear region and time projection (right; scale bar, 1 μm). Pseudocolor mode represents the FRET/CFP ratio ($n = 10$ independent experiments). **e**, Frequency distribution of Rab11$^+$ vesicle displacement from the origin in cells expressing GFP-Rab11^{S25N} or GFP-Rab11 treated with either vehicle (DMSO), nocodazole (a microtubule depolymerizing drug) or the dynein inhibitor, ciliobrevin D ($n = 4$ independent experiments; $^{***}P < 0.005$; $^{*}P < 0.05$; two-way ANOVA). **f**, Quantification of Rab11 activation in the perinuclear area. Cells were treated with either vehicle (DMSO) or nocodazole ($n = 14$ independent experiments; data represent mean ± s.e.m.; $^{**}P < 0.01$; two-tailed unpaired *t*-test). **g**, Quantification of Rab11 activation in the perinuclear area. Cells were treated with either vehicle (DMSO) or ciliobrevin D ($n = 14$ independent experiments; data represent mean ± s.e.m.; $^{**}P < 0.01$; *t*-test). **h**, Frequency distribution of linearity of movement of Rab11$^+$ vesicles in cells expressing GFP-Rab11^{S25N} or GFP-Rab11 treated with either vehicle (DMSO), nocodazole or ciliobrevin D ($n = 4$ independent experiments; data represent mean ± s.e.m.; $^{***}P < 0.005$; two-way ANOVA). **i**, Representative image of endocytosed transferrin localization in cells expressing GFP-Rab11^{S25N} or GFP-Rab11 treated with either vehicle (DMSO), nocodazole, or ciliobrevin D ($n = 4$ independent experiments). Scale bar, 10 μm. **j**, Quantification of perinuclear localization of fluorescent transferrin in cells expressing GFP-Rab11^{S25N} or treated with either DMSO/scramble siRNA, Rab11 siRNA 1 (RAB11-KD$_1$), Rab11 siRNA 2 (RAB11-KD$_2$), nocodazole or the dynein inhibitor, ciliobrevin D ($n = 12$ independent experiments; data represent mean ± s.e.m.; $^{***}P < 0.005$; one-way ANOVA).

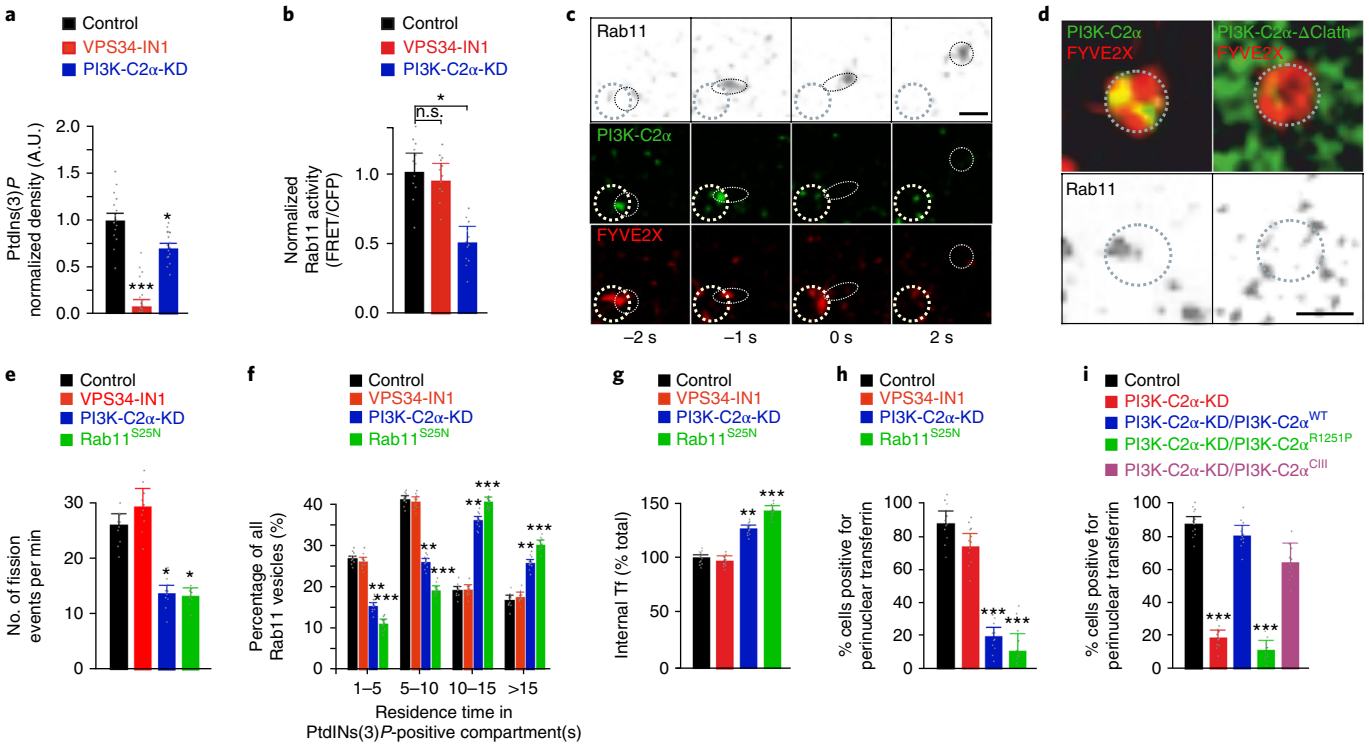

Fig. 4 | PI3K-C2α-dependent Rab11 activation on PtdIns(3)P-positive endosomes. a, Quantification of PtdIns(3)P abundance in COS-7 cells treated with either DMSO/Scramble siRNA (control), VPS34 inhibitor (VPS34-IN1), or PI3K-C2α siRNA (PI3KC2α-KD) ($n=15$ independent experiments; data represent mean ± s.e.m.; $^{***}P<0.005$, $^{*}P<0.05$; one-way ANOVA). **b**, Quantification of Rab11 activity in COS-7 cells treated with either DMSO/Scramble siRNA (control), VPS34 inhibitor (VPS34-IN1), or PI3K-C2α siRNA (PI3KC2α-KD). ($n=12$ independent experiments; data represent mean ± s.e.m.; $^{*}P<0.05$; one-way ANOVA). **c**, Representative time-lapse series of cells co-expressing mCherry-FYVE2X, GFP-PI3K-C2α, and mECFP-Rab11 (gray scale). White circles represent membrane-bound structures ($n=6$ independent experiments). Scale bar, 1 µm. **d**, Representative image of cells co-expressing mCherry-FYVE2X, mECFP-Rab11 (gray scale) and GFP-PI3K-C2α (PI3K-C2α) or its mutant version GFP-PI3K-C2α-Δclathrin (PI3K-C2α-ΔClath). White circles represent membrane-bound structures ($n=6$ independent experiments). Scale bar, 1 µm. **e**, Quantification of the number of Rab11-associated fission events generated from mCherry-FYVE2X-positive membranes. COS-7 cells expressing GFP-Rab11^{S25N} or GFP-Rab11 treated with either DMSO/Scramble siRNA (control), VPS34 inhibitor (VPS34-IN1), or PI3K-C2α siRNA (PI3KC2α-KD, blue bar). ($n=10$ independent experiments; data represent mean ± s.e.m.; $^{*}P<0.05$; one-way ANOVA). **f**, Residence time of GFP-Rab11^{S25N} or GFP-Rab11 structures on mCherry-FYVE2X-positive membranes (black, blue, and red bars). GFP-Rab11-expressing cells were treated with either DMSO/Scramble siRNA (control), VPS34 inhibitor (VPS34-IN1), or PI3K-C2α siRNA (PI3KC2α-KD). ($n=10$ independent experiments; data represent mean ± s.e.m.; $^{***}P<0.005$, $^{**}P<0.01$; two-way ANOVA.) **g**, Quantification of internal transferrin percentage in cells expressing GFP-Rab11^{S25N} or GFP-Rab11 treated with either DMSO/Scramble siRNA (control), VPS34 inhibitor (VPS34-IN1), or PI3K-C2α siRNA (PI3KC2α-KD). ($n=12$ independent experiments; data represent mean ± s.e.m.; $^{**}P<0.01$, $^{***}P<0.005$; one-way ANOVA). **h**, Quantification of perinuclear localization of fluorescent transferrin in cells expressing GFP-Rab11^{S25N} or GFP-Rab11 treated with either DMSO/Scramble siRNA (control), VPS34 inhibitor (VPS34-IN1), or PI3K-C2α siRNA (PI3KC2α-KD) ($n=12$ independent experiments; data represent mean ± s.e.m.; $^{***}P<0.005$; one-way ANOVA). **i**, Quantification of perinuclear localization of fluorescent transferrin in cells expressing GFP-Rab11 treated with either DMSO/Scramble siRNA (control), PI3K-C2α siRNA (PI3KC2α-KD), PI3K-C2α siRNA and PI3K-C2α^{wt} siRNA-resistant (PI3KC2α-KD/ PI3KC2α^{wt}), PI3K-C2α siRNA and PI3K-C2α^{R1251P} siRNA resistant (PI3KC2α-KD/ PI3KC2α^{1251}), or PI3K-C2α siRNA and PI3K-C2α^{CIII} siRNA resistant (PI3KC2α-KD/ PI3KC2α^{CIII}) ($n=12$ independent experiments; data represent mean ± s.e.m.; $^{***}P<0.005$; one-way ANOVA).

ciliobrevin D treatments decreased juxtanuclear accumulation of endocytosed transferrin (Fig. 3i,j).

Overall, these data indicate that the transferrin receptor is removed from PEs and transported to the ERC through a local increase of PtdIns(3)*P*, the activation of Rab11, the hydrolysis of PtdIns(3)*P*, and eventually the dynein-mediated vesicular transport.

PI3K-C2α controls Rab11 activity on PtdIns(3)P⁺ endosomes. In early endosomes, PtdIns(3)*P* is mainly produced by class III PI3K. However, a small but significant amount of PtdIns(3)*P*, ranging up to 20%, derives from class II PI3Ks[39] and is putatively required for Rab11 activation[9,10]. To further determine whether the activation of Rab11 preferentially depended on either class II or III PI3K, we studied modulation of the AS-Rab11 probe after either PI3K-C2α or Vps34 knockdown or Vps34 inhibition (Supplementary Fig. 6a–c). As expected, knockdown of PI3K-C2α induced a 20% loss of PtdIns(3)*P*, as well as a 50% drop in Rab11 activity (Fig. 4a,b). By contrast, knockdown or inhibition of Vps34 by VPS34-IN1 decreased PtdIns(3)*P* cell content by 80% but failed to significantly reduce the levels of active Rab11 (Fig. 4a,b). This highlights the distinct role of PI3K-C2α in controlling Rab11 activity in PE. In addition, PI3K-C2α localization during cargo release from PtdIns(3)*P*⁺ structures was imaged. GFP-PI3K-C2α colocalized with mCherry-FYVE2X during the fission of mECFP-Rab11-positive structures (Fig. 4c; Supplementary Fig. 6d–f), whereas it was undetected in the newly formed mECFP-Rab11⁺/mCherry-TfR⁺ membranes (Supplementary Fig. 6e–g). Interestingly, such PI3K-C2α localization strictly depended on its N-terminal clathrin-binding domain[40], as loss of this domain[41] resulted in a diffuse cytosolic distribution around the PE (Fig. 4d).

Number, displacement, and direction of Rab11-positive vesicles leaving PEs were analyzed in PI3K-C2α-knockdown cells to further

characterize the role of PI3K-C2α in the control of Rab11-mediated intracellular trafficking. Reduction in the abundance of PI3K-C2α, as well as the expression of GFP-Rab11^{S25N}, lowered the number of Rab11$^+$ vesicles emerging from PEs (Fig. 4e). Furthermore, increased residence time of Rab11 at the PEs was observed in both PI3K-C2α-KD- and Rab11^{S25N}-expressing cells (Fig. 4f). On the contrary, pharmacological inhibition of Vps34 did not alter either the number of fission events or the residence time of Rab11 on PEs (Fig. 4e,f), strengthening the idea that Vps34 and PI3K-C2α present nonredundant functions during the endocytic recycling of transferrin.

Next, to further confirm this evidence, quantitation and localization of labeled Tf were performed. PI3K-C2α-KD and GFP-Rab11^{S25N}-expressing cells displayed increased Tf accumulation and decreased Tf perinuclear storage, which was not affected by inhibition or RNA interference (RNAi)-mediated suppression of Vps34 (Fig. 4g,h; Supplementary Fig. 6c,h). Such a delay in transferrin recycling did not depend on the efficiency of molecular motors, as a similar distribution of linearity and vesicle speed between GFP-Rab11^{S25N}-expressing cells, PI3K-C2α-KD and controls were measured by tracking of individual Rab11$^+$ vesicles (Supplementary Fig. 6i,j). This Tf delivery defect in PI3K-C2α-KD cells was rescued by expression of a wild-type (PI3K-C2α^{WT}) or a PI3P-only producing PI3K-C2α form (PI3K-C2α^{CIII}) (Fig. 4i). In contrast, expression of a kinase-inactive mutant (PI3K-C2α^{R1251P}) did not restore juxtanuclear Tf localization (Fig. 4i), thus demonstrating that Tf delivery to perinuclear endosomes is controlled by the PI3K-C2α-dependent PI3P production. In line with these results, silencing of PI3K-C2α led to the intracellular entrapment of Tf (Supplementary Fig. 6k).

Altogether, these results indicated that removal of recycling cargo from early endosomes requires PI3K-C2α-mediated PI3P production, which is necessary for Rab11 activation. Nonetheless, PtdIns(3)*P* decreased prior fission and disappeared from the detached Rab11$^+$ vesicle, suggesting that removal of recycling cargo from endosomes depends on PtdIns(3)*P* hydrolysis.

The PtdIns(3)*P* phosphatase MTM1 is a Rab11 effector. To identify the PtdIns(3)*P* phosphatase that connects the increase in Rab11 activity with the concomitant decrease of PtdIns(3)*P*, we performed pull-down assays of potential PtdIns(3)*P* phosphatases working as Rab11 effectors. Five different PtdIns(3)*P* phosphatases, members of the myotubularin protein family, were tested using immobilized glutathione *S*-transferase (GST)-Rab11 as a probe. Among them, MTM1 was found to preferentially bind Rab11:GTP-γS rather than Rab11:GDP (Fig. 5a). On the contrary, no interactions were detected for MTMR2, MTMR4, MTMR6, and MTMR9 (Fig. 5a). Remarkably, MTM1 was isolated from total cell extracts by pull-down of Rab11-GTP using a recombinant Rab11-GTP-interacting protein (GST-RBD11) as a probe[9] (Fig. 5b) and by immunoprecipitation of endogenous Rab11 (Supplementary Fig. 7a), thus indicating that Rab11 is associated with MTM1 in vivo. In further agreement, an in vitro binding assay using purified GST-Rab11 and His-Flag-MTM1 showed preferential binding of recombinant MTM1 with Rab11:GTP-γS compared to Rab11:GDP or other Rabs (Fig. 5c; Supplementary Fig. 7b). RNAi-mediated downregulation of MTM1 (MTM1-KD) (Supplementary Fig. 7c) significantly increased levels of PtdIns(3)*P* as well as activity of Rab11 (Fig. 5d,e). In MTM1-KD cells, additional silencing of PI3K-C2α, but not of Vps34, reduced Rab11 activation (Fig. 5e). These results indicate that active Rab11 is associated with the PtdIns(3)*P* phosphatase MTM1, which actively dephosphorylates the PtdIns(3)*P* present on the structures directed toward the ERC. In agreement with this view, confocal microscopy analysis showed that Rab11 and MTM1 colocalized in both the PE and the ERC membranes, as well as in TfR$^+$ vesicles (Fig. 5f,g; Supplementary Fig. 7d). In line with these results, Rab11 silencing blocked perinuclear and peripheral MTM1 localization (Supplementary Fig. 7e).

To further characterize the impact of MTM1 in the control of Rab11-mediated intracellular trafficking, we analyzed Rab11$^+$ vesicles detaching from PEs after RNAi-mediated downregulation of MTM1 (MTM1-KD). Loss of MTM1 as well as expression of GFP-Rab11^{S25N} decreased the number of Rab11-positive fission events from PEs (Fig. 5h) without affecting vesicle speed (Supplementary Fig. 7f). Furthermore, the residence time of Rab11-positive structures on PEs increased in both conditions (Fig. 5i). Therefore, either impaired activation of Rab11 or lack of the phosphatase activity delayed fission. In agreement with this theory, MTM1-KD and GFP-Rab11^{S25N}-expressing cells displayed increased Tf content and decreased perinuclear accumulation of the recycling cargo (Fig. 5j,k; Supplementary Fig. 7g). To identify the lipid kinase that antagonizes MTM1 activity, we performed the rescue of Tf uptake and Tf accumulation of the recycling cargo at the ERC. Acute perturbation of PtdIns(3)*P* synthesis by inhibition of Vps34 partially restored Tf accumulation and perinuclear storage in MTM1-KD cells (Fig. 5j,k) without affecting the increase in Rab11 activation due to MTM1 loss (Fig. 5e). In agreement, Rab11-mediated fission events appeared more frequently in MTM1-KD/VPS34-IN1 than in MTM1-KD cells (Fig. 5h), thus indicating that fission requires a substantial reduction of PtdIns(3)*P*. In the absence of MTM1, knockdown of either PI3K-C2α alone or in combination with Vps34 inhibition led to decreased Rab11 activity. Conversely, in the absence of MTM1, Vps34 inhibition alone was not able to restore increased Rab11 activity (Fig. 5e). Therefore, PI3K-C2α is the main kinase driving the production of PtdIns(3)*P* required for Rab11 activation, consequent fission, and Tf recycling (Fig. 5h,j,k).

Taken together, these results show that removal of recycling cargo from peripheral endosomes depends on subsequent PI3K-C2α-mediated PtdIns(3)*P* production, Rab11 activation and MTM1-dependent PtdIns(3)*P* destruction, leading to fission of vesicles and their eventual dynein-mediated transport to the ERC.

Discussion

Removal of recycling cargo from the peripheral PtdIns(3)*P*$^+$ endosome requires hydrolysis of PtdIns(3)*P* and the activation of the small GTPase Rab11. However, whether these events are linked is unknown. Therefore, a genetically-encoded FRET biosensor for Rab11 was generated to detect spatial and temporal variations of Rab11 activity in endosomes. This biosensor, named AS-Rab11, was proven to be effective in limited diffusional space, such as in membrane and vesicular compartments, and its activity was found to depend on both positive and negative Rab11 regulators, such as Rab11 GEF, GAP and GDI[34–36]. Using AS-Rab11, we revealed that: (1) Rab11 activation is initiated on PtdIns(3)*P*-positive membranes where sorting of recycling cargo occurs; (2) the Rab11 activation level determines the release rate of membranes destined to the ERC; and (3) such release required MTM1, a PtdIns(3)*P* phosphatase, which was found to interact with active Rab11. These results establish that removal of recycling cargo from peripheral PtdIns(3)*P*$^+$ endosome requires coupling of Rab11 activity and PtdIns(3)*P* turnover (Fig. 6).

Extensive time-lapse analyses and biochemical experiments revealed enrichment of active Rab11 on juxtanuclear-positioned ERC and peripheral PtdIns(3)*P*$^+$ endocytic structures. In addition, a critical role for activated Rab11 in the release of transferrin receptors (TfR) from PtdIns(3)*P*$^+$ membranes was found. Given that PtdIns(3)*P* is a bona fide marker[18] of EE, a compartment where recycling cargoes are sorted and directed toward the ERC or plasma membrane[14,28], our data suggest that Rab11 activation is initiated on EE membranes in which sorting of recycling cargoes occurs. In agreement, the direct visualization of active Rab11 patches localizing with TfR on PtdIns(3)*P*$^+$ membranes corroborate this evidence. Our experiments show that membranes decorated by active Rab11 are not maintained indefinitely

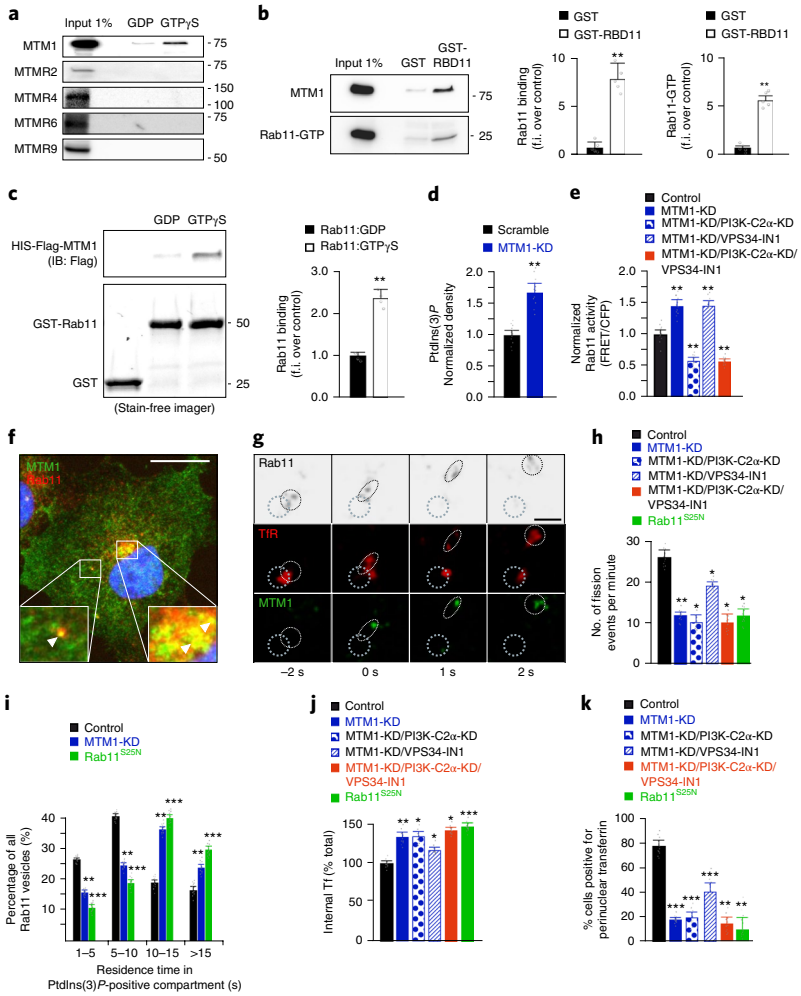

Fig. 5 | The PtdIns(3)*P* phosphatase MTM1 is a Rab11 effector. a, Affinity chromatography of Rab11-GTP effectors. Representative western blot of both Rab11-GDP and Rab11-GTPγS column eluate probed with anti-MTM1, anti-MTMR2, anti-MTMR4, anti-MTMR6, and anti-MTMR9 antibodies ($n=5$ independent experiments; uncropped blots are shown in Supplementary Fig. 8). **b**, Pull down of the endogenous Rab11-GTP and MTM1 complex. Representative western blot of Rab11-GTP pull-down assay probed with anti-MTM1 antibody ($n=5$ independent experiments). Quantification of endogenous MTM1 (center) and Rab11-GTP (right) pulled down by GST or GST-RBD11 probe ($n=5$ independent experiments; data represent mean ± s.e.m.; $^{**}P<0.01$; two-tailed unpaired *t*-test; uncropped blots are shown in Supplementary Fig. 8). **c**, In vitro assessment of the association between recombinant Rab11-GTP and MTM1. left, representative western blot of recombinant Rab11 loaded with GDP or GTPγS and probed for MTM1 interaction. Right, quantification of recombinant MTM1 pulled down by recombinant Rab11 loaded with GDP or GTPγS ($n=4$ independent experiments, data represent mean ± s.e.m.; $^{**}P<0.01$; *t*-test; uncropped blots are shown in Supplementary Fig. 8). **d**, Quantification of PtdIns(3)P abundance in COS-7 cells treated with either Scramble siRNA (control) or MTM1 siRNA (MTM1-KD). ($n=12$ independent experiments; data represent mean ± s.e.m.; $^{**}P<0.01$, *t*-test.) **e**, Quantification of active Rab11 levels in COS-7 cells treated with either Scramble siRNA (control), MTM1 siRNA (MTM1-KD), MTM1 siRNA and PI3K-C2α siRNA (MTM1-KD/PI3K-C2α-KD), MTM1 siRNA and VPS34 inhibitor (MTM1-KD/VPS34-IN1), or MTM1 siRNA in combination with PI3K-C2α siRNA and VPS34 inhibitor (MTM1-KD/PI3K-C2α-KD/VPS34-IN1). ($n=12$ independent experiments; data represent mean ± s.e.m.; $^{**}P<0.01$; one-way ANOVA.) **f**, Representative immunofluorescence of COS-7 cells, showing peripheral and perinuclear colocalization of MTM1 with Rab11. Peripheral (left) and perinuclear (right) magnification are shown at the bottom ($n=6$ independent experiments). White arrows highlight colocalization. Scale bar, 15 µm. **g**, Representative time-lapse series of cells co-expressing mCherry-transferrin receptor (TfR), mECFP-Rab11 (gray scale) and GFP-MTM1. White circles represent membrane-bound structures ($n=6$ independent experiments). Scale bar, 1 µm. **h**, Quantification of the number of Rab11-associated fission events generated from mCherry-FYVE2X-positive membranes. Cells expressing GFP-Rab11^{S25N} or GFP-Rab11 treated with either DMSO/Scramble siRNA (control), MTM1 siRNA (MTM1-KD), MTM1 siRNA and PI3K-C2α siRNA (MTM1-KD/PI3K-C2α-KD), MTM1 siRNA and VPS34 inhibitor (MTM1-KD/VPS34-IN1), or MTM1 siRNA in combination with PI3K-C2α siRNA and VPS34 inhibitor (MTM1-KD/PI3K-C2α-KD/VPS34-IN1) ($n=12$ independent experiments; data represent mean ± s.e.m., $^{**}P<0.01$, $^{*}P<0.05$; one-way ANOVA). **i**, Residence time of GFP-Rab11^{S25N} or GFP-Rab11 structures on mCherry-FYVE2X-positive membranes (black and blue bars). Cells expressing GFP-Rab11 were treated with either Scramble siRNA (control) or MTM1 siRNA (MTM1-KD). ($n=12$ independent experiments; data represent mean ± s.e.m.; $^{***}P<0.005$, $^{**}P<0.01$, two-way ANOVA). **j**, Quantification of internal transferrin percentage in COS-7 cells expressing GFP-Rab11^{S25N} or GFP-Rab11 treated with either DMSO/Scramble siRNA (control), MTM1 siRNA (MTM1-KD), MTM1 siRNA and PI3K-C2α siRNA (MTM1-KD/PI3K-C2α-KD), MTM1 siRNA and VPS34 inhibitor (MTM1-KD/VPS34-IN1), or MTM1 siRNA in combination with PI3K-C2α siRNA and VPS34 inhibitor (MTM1-KD/PI3K-C2α-KD/VPS34-IN1) ($n=12$ independent experiments; data represent mean ± s.e.m.; $^{***}P<0.005$, $^{**}P<0.01$, $^{*}P<0.05$; one-way ANOVA). **k**, Quantification of perinuclear localization of fluorescent transferrin in COS-7 cells expressing GFP-Rab11^{S25N} or GFP-Rab11 treated with either DMSO/Scramble siRNA (control), MTM1 siRNA (MTM1-KD), MTM1 siRNA and PI3K-C2α siRNA (MTM1-KD/PI3K-C2α -KD), MTM1 siRNA and VPS34 inhibitor (MTM1-KD/VPS34-IN1), or MTM1 siRNA in combination with PI3K-C2α siRNA and VPS34 inhibitor (MTM1-KD/PI3K-C2α-KD/VPS34-IN1) ($n=12$ independent experiments; data represent mean ± s.e.m.; $^{***}P<0.005$, $^{**}P<0.01$; one-way ANOVA).

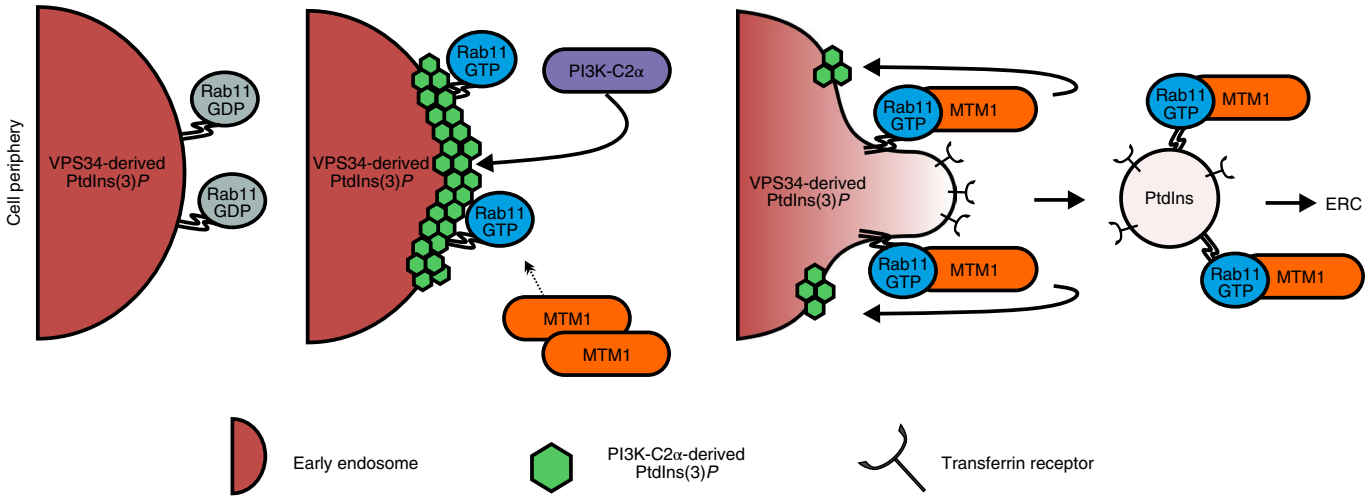

Fig. 6 | Trafficking of recycling cargo from peripheral endosome to ERC requires Rab11 activation and PtdIns(3)P turnover. On a peripheral PtdIns(3)*P* membrane a transient and local burst of PI3K-C2α-derived PtdIns(3)*P* triggers Rab11 activation (first and second panel from the left). Active Rab11 (Rab11-GTP) recruits MTM1, a PtdIns(3)*P* phosphatase, which catalyzes PtdIns(3)*P* hydrolysis (third panel from the left). PtdIns(3)*P* reduction allows vesicle fission and trafficking of cargo toward the ERC (rightmost panel).

on PtdIns(3)P^+ structures but are delivered from peripheral to juxtanuclear recycling compartments. These observations define that, differently from active Rab5 that mediates the expansion of Rab5 domain on early endosomes, active Rab11 critically affects cargo flow by recruiting the protein machinery involved in vesicle transport. In line with this view, our results show that active Rab11 vesicles detaching from peripheral endosomes accumulate on ERC membranes in a dynein-dependent manner.

Our observations extend the previous identification of PI3K-C2α as a key controller of Rab11 activation on endosomes[9] and define that localization of PI3K-C2α on endosomes strictly depends on its clathrin-binding domain[20,40]. Notably, depletion of PI3K-C2α delays the kinetic of vesicle release from the PtdIns(3)P^+ structure, where TfR sorting takes place[1], thus linking the role of PI3K-C2α to endosomal sorting. Accordingly, depletion of PI3K-C2α, as well as loss of its catalytic activity, decreases both activity and fission of Rab11-positive vesicles from PtdIns(3)P^+ structures, thereby mimicking the phenotype observed in cells expressing dominant negative Rab11.

In light of the highly dynamic Rab11 activation on PtdIns(3)P^+ structures, and the distinct phosphoinositide composition of EE and the perinuclear recycling compartment[42], a phosphoinositide conversion can be expected between these two Rab11-positive membrane domains. Our data demonstrated that this transition is controlled by MTM1, which was found to interact with active Rab11. MTM1 was shown to antagonize the class II and class III-derived PtdIns(3)*P* pools in *D. melanogaster* and *C. elegans* and was demonstrated to be essential in the exit of cargos from PtdIns(3)*P* endosomes[8,26]. Accordingly, MTM1$^+$/Rab11$^+$ vesicles were observed during removal of recycling cargo from the PtdIns(3)*P* compartment, thus indicating that active Rab11 provides a signal to control MTM1 localization. Given that recycling vesicles require dynein to reach the ERC, removal of PI3P can be explained by the fact that the presence of this lipid, a well-known activator of centrifugal kinesin-mediated transport[43], might disturb this centripetal trafficking.

The development and application of AS-Rab11 to quantitatively analyze Rab11 activity in living cells allowed dissection and analysis of the initial step of the PtdIns conversion mechanism[42] required for the exit of recycling cargo from endosomes. Our data indicate that PI3K-C2α provides a spatially localized and temporally controlled PtdIns(3)*P* pool that is sufficient to activate Rab11 on early endosomes, allowing the establishment and maintenance of receptor recycling toward the ERC. Activation of Rab11 eventually contributes to the recruitment of MTM1 and the ensuing reduction of PtdIns(3)*P* level on membranes destined to the perinuclear endosome.

Methods

Methods, including statements of data availability and any associated accession codes and references, are available at https://doi.org/10.1038/s41589-018-0086-4.

Received: 13 September 2017; Accepted: 10 May 2018;
Published online: 18 June 2018

References

1. Maxfield, F. R. & McGraw, T. E. Endocytic recycling. *Nat. Rev. Mol. Cell Biol.* **5**, 121–132 (2004).
2. Cullen, P. J. Endosomal sorting and signalling: an emerging role for sorting nexins. *Nat. Rev. Mol. Cell Biol.* **9**, 574–582 (2008).
3. Mellman, I. & Nelson, W. J. Coordinated protein sorting, targeting and distribution in polarized cells. *Nat. Rev. Mol. Cell Biol.* **9**, 833–845 (2008).
4. Jovic, M., Sharma, M., Rahajeng, J. & Caplan, S. The early endosome: a busy sorting station for proteins at the crossroads. *Histol. Histopathol.* **25**, 99–112 (2010).
5. Takahashi, S. et al. Rab11 regulates exocytosis of recycling vesicles at the plasma membrane. *J. Cell Sci.* **125**, 4049–4057 (2012).
6. Winter, J. F. et al. *Caenorhabditis elegans* screen reveals role of PAR-5 in RAB-11-recycling endosome positioning and apicobasal cell polarity. *Nat. Cell Biol.* **14**, 666–676 (2012).
7. Jović, M. et al. Endosomal sorting of VAMP3 is regulated by PI4K2A. *J. Cell Sci.* **127**, 3745–3756 (2014).
8. Ketel, K. et al. A phosphoinositide conversion mechanism for exit from endosomes. *Nature* **529**, 408–412 (2016).
9. Franco, I. et al. PI3K class II α controls spatially restricted endosomal PtdIns3P and Rab11 activation to promote primary cilium function. *Dev. Cell* **28**, 647–658 (2014).
10. Franco, I. et al. Phosphoinositide 3-kinase-C2α regulates polycystin-2 ciliary entry and protects against kidney cyst formation. *J. Am. Soc. Nephrol.* **27**, 1135–1144 (2016).
11. Horgan, C. P., Hanscom, S. R., Jolly, R. S., Futter, C. E. & McCaffrey, M. W. Rab11-FIP3 binds dynein light intermediate chain 2 and its overexpression fragments the Golgi complex. *Biochem. Biophys. Res. Commun.* **394**, 387–392 (2010).
12. Horgan, C. P., Hanscom, S. R., Jolly, R. S., Futter, C. E. & McCaffrey, M. W. Rab11-FIP3 links the Rab11 GTPase and cytoplasmic dynein to mediate transport to the endosomal-recycling compartment. *J. Cell Sci.* **123**, 181–191 (2010).

13. Ren, M. et al. Hydrolysis of GTP on rab11 is required for the direct delivery of transferrin from the pericentriolar recycling compartment to the cell surface but not from sorting endosomes. *Proc. Natl. Acad. Sci. USA* **95**, 6187–6192 (1998).
14. Ullrich, O., Reinsch, S., Urbé, S., Zerial, M. & Parton, R. G. Rab11 regulates recycling through the pericentriolar recycling endosome. *J. Cell Biol.* **135**, 913–924 (1996).
15. Traer, C. J. et al. SNX4 coordinates endosomal sorting of TfnR with dynein-mediated transport into the endocytic recycling compartment. *Nat. Cell Biol.* **9**, 1370–1380 (2007).
16. Sönnichsen, B., De Renzis, S., Nielsen, E., Rietdorf, J. & Zerial, M. Distinct membrane domains on endosomes in the recycling pathway visualized by multicolor imaging of Rab4, Rab5, and Rab11. *J. Cell Biol.* **149**, 901–914 (2000).
17. Balla, T. Phosphoinositides: tiny lipids with giant impact on cell regulation. *Physiol. Rev.* **93**, 1019–1137 (2013).
18. Simonsen, A. et al. EEA1 links PI(3)K function to Rab5 regulation of endosome fusion. *Nature* **394**, 494–498 (1998).
19. Braccini, L. et al. PI3K-C2γ is a Rab5 effector selectively controlling endosomal Akt2 activation downstream of insulin signalling. *Nat. Commun.* **6**, 7400 (2015).
20. Campa, C. C., Franco, I. & Hirsch, E. PI3K-C2α: one enzyme for two products coupling vesicle trafficking and signal transduction. *FEBS Lett.* **589**, 1552–1558 (2015).
21. Backer, J. M. The regulation and function of class III PI3Ks: novel roles for Vps34. *Biochem. J.* 410, (1–17 (2008).
22. Jean, S., Cox, S., Schmidt, E. J., Robinson, F. L. & Kiger, A. Sbf/MTMR13 coordinates PI(3)P and Rab21 regulation in endocytic control of cellular remodeling. *Mol. Biol. Cell* **23**, 2723–2740 (2012).
23. Cao, C., Backer, J. M., Laporte, J., Bedrick, E. J. & Wandinger-Ness, A. Sequential actions of myotubularin lipid phosphatases regulate endosomal PI(3)P and growth factor receptor trafficking. *Mol. Biol. Cell* **19**, 3334–3346 (2008).
24. Cao, C., Laporte, J., Backer, J. M., Wandinger-Ness, A. & Stein, M. P. Myotubularin lipid phosphatase binds the hVPS15/hVPS34 lipid kinase complex on endosomes. *Traffic* **8**, 1052–1067 (2007).
25. Hnia, K., Vaccari, I., Bolino, A. & Laporte, J. Myotubularin phosphoinositide phosphatases: cellular functions and disease pathophysiology. *Trends Mol. Med.* **18**, 317–327 (2012).
26. Velichkova, M. et al. *Drosophila* Mtm and class II PI3K coregulate a PI(3)P pool with cortical and endolysosomal functions. *J. Cell Biol.* **190**, 407–425 (2010).
27. Wandinger-Ness, A. & Zerial, M. Rab proteins and the compartmentalization of the endosomal system. *Cold Spring Harb. Perspect. Biol.* **6**, a022616 (2014).
28. Campa, C. C. & Hirsch, E. Rab11 and phosphoinositides: A synergy of signal transducers in the control of vesicular trafficking. *Adv. Biol. Regul.* **63**, 132–139 (2017).
29. Lu, Q. et al. Early steps in primary cilium assembly require EHD1/EHD3-dependent ciliary vesicle formation. *Nat. Cell Biol.* **17**, 531 (2015).
30. Welz, T., Wellbourne-Wood, J. & Kerkhoff, E. Orchestration of cell surface proteins by Rab11. *Trends Cell Biol.* **24**, 407–415 (2014).
31. Eathiraj, S., Mishra, A., Prekeris, R. & Lambright, D. G. Structural basis for Rab11-mediated recruitment of FIP3 to recycling endosomes. *J. Mol. Biol.* **364**, 121–135 (2006).
32. Miyawaki, A. & Tsien, R. Y. Monitoring protein conformations and interactions by fluorescence resonance energy transfer between mutants of green fluorescent protein. *Methods Enzymol.* **327**, 472–500 (2000).
33. Pertz, O., Hodgson, L., Klemke, R. L. & Hahn, K. M. Spatiotemporal dynamics of RhoA activity in migrating cells. *Nature* **440**, 1069–1072 (2006).
34. Sakaguchi, A. et al. REI-1 Is a guanine nucleotide exchange factor regulating RAB-11 localization and function in *C. elegans* embryos. *Dev. Cell* **35**, 211–221 (2015).
35. Gallo, L. I. et al. TBC1D9B functions as a GTPase-activating protein for Rab11a in polarized MDCK cells. *Mol. Biol. Cell* **25**, 3779–3797 (2014).
36. Chen, W., Feng, Y., Chen, D. & Wandinger-Ness, A. Rab11 is required for trans-golgi network-to-plasma membrane transport and a preferential target for GDP dissociation inhibitor. *Mol. Biol. Cell* **9**, 3241–3257 (1998).
37. Firestone, A. J. et al. Small-molecule inhibitors of the AAA+ ATPase motor cytoplasmic dynein. *Nature* **484**, 125–129 (2012).
38. Delevoye, C. et al. Recycling endosome tubule morphogenesis from sorting endosomes requires the kinesin motor KIF13A. *Cell Reports* **6**, 445–454 (2014).
39. Devereaux, K. et al. Regulation of mammalian autophagy by class II and III PI 3-kinases through PI3P synthesis. *PLoS One* **8**, e76405 (2013).
40. Gaidarov, I., Smith, M. E., Domin, J. & Keen, J. H. The class II phosphoinositide 3-kinase C2α is activated by clathrin and regulates clathrin-mediated membrane trafficking. *Mol. Cell* **7**, 443–449 (2001).
41. Gulluni, F. et al. Mitotic spindle assembly and genomic stability in breast cancer require PI3K–C2α scaffolding function. *Cancer Cell* **32**, 444–459.e7 (2017).
42. Marat, A. L. & Haucke, V. Phosphatidylinositol 3-phosphates-at the interface between cell signalling and membrane traffic. *EMBO J.* **35**, 561–579 (2016).
43. Hoepfner, S. et al. Modulation of receptor recycling and degradation by the endosomal kinesin KIF16B. *Cell* **121**, 437–450 (2005).

Acknowledgements

We are grateful to C. Bucci from University of Salento, K. Sato from University of Gunma, G. Apodaca from University of Pittsburgh, M. Bonazzi from University of Montpellier, J. Laporte from Institut de Génétique et de Biologie Moléculaire et Cellulaire (IGBMC), L. Lanzetti from Candiolo Cancer Institute and S. Sigismund, G. Scita and A. Palamidessi from Fondazione Istituto FIRC di Oncologia Molecolare (IFOM) for providing reagents. We are grateful to M. Gai from University of Turin for providing technical support in confocal microscopy. This work was supported by Associazione Italiana Ricerca sul Cancro (AIRC) (161813), Compagnia di San Paolo, Wold Wide Cancer Research Association (151324) and "Futuro e Ricerca 2010" (RBFR10HP97_004). C.C.C. was supported by a FIRC (Fondazione italiana ricerca sul cancro) research fellowship. J.P.M. was supported by a UIF (Università Italo-Francese) co-tutele Phd programme.

Author contributions

C.C.C., J.P.M., and E.H. conceived and designed the experiments. C.C.C., M.C.D.S., L.G., and F.C. performed in vitro experiments and analyzed the data; J.P.M., C.C.C., and A.D., performed in vitro experiments and analyzed the data; M.D.G. and C.B. analyzed imaging data; C.C.C. and E.H. wrote the manuscript. All authors contributed to data interpretation. All authors reviewed the paper and provided comments.

Competing interests

E.H. is a co-founder of Kither Biotech, a company involved in the development of PI3K inhibitors.

Additional information

Supplementary information is available for this paper at https://doi.org/10.1038/s41589-018-0086-4.

Reprints and permissions information is available at www.nature.com/reprints.

Correspondence and requests for materials should be addressed to C.C.C. or E.H.

Publisher's note: Springer Nature remains neutral with regard to jurisdictional claims in published maps and institutional affiliations.

Methods

Antibodies. The following antibodies were used in this study: mouse-anti-PI3K-C2α (BD Biosciences 611046, western blotting (WB) 1:500); mouse-anti-Rab11 (BD Biosciences 610656, WB 1:1,000); rabbit-anti-MTM1 (SIGMA HPA010008, WB 1:1,000); mouse-anti-FLAG (SIGMA clone M2, WB 1:2,000); mouse-anti-GFP (Abcam ab127417, WB 1:1,000); rabbit-anti-VPS34 (Novus Biologicals NB110-87320SS, WB 1:1,000); mouse-anti-MTMR4 (Santa Cruz sc-373922, WB 1:500); mouse-anti-MTMR6 (Abcam ab69875, WB 1:1,000); mouse-anti-MTMR9 (Santa Cruz sc-514366, WB 1:1,000); rabbit-anti-FIP2 (Abcam ab76892, WB 1:1,000); rabbit-anti-FIP4 (Biorbyt orb215321, WB 1:1,000). The following peroxidase-linked secondary antibodies were used: Anti-mouse IgG (ab131368, WB 1:5,000) and Anti-Rabbit IgG (A0545 SIGMA, 1:5,000). The following Alexa-Fluor conjugated secondary antibodies were used: anti-mouse/rabbit IgG Alexa Fluor 488/568 (IF 1:1,000).

SiRNA and plasmid transfection. All siRNAs used in this study were 21-, 23-, or 27-base oligonucleotides including 3′-dTdT overhangs. For silencing, the following siRNAs were used targeting the human isoform: PI3K-C2α 5′-GGCAAGATATGTTAGCTTT-3′ and MTM1 5′-GATGCAAGACCCAGCGTAA-3′. The scrambled control siRNA used throughout this study corresponded to the sequence 5′-ATGAGTTAGATGCGTTCTA-3′.

COS-7 cells were transfected with siRNA using Lipofectamine 2000 (Invitrogen) according to the manufacturer's protocol. To achieve optimal knockdown efficiency, two rounds of silencing were performed. Cells were transfected on day 1, expanded on day 2 and seeded for the experiment on day 3; the experiment was performed on day 4.

For transient overexpression of proteins in silenced cells, plasmids were transfected on day 4 12 h before analysis using Lipofectamine 2000 (Invitrogen). For transient overexpression of proteins in untreated cells, plasmids were transfected 12 h before analysis using Lipofectamine 2000 (Invitrogen).

Recombinant protein production. GST-Rab11a recombinant protein was generated by cloning Rab11a cDNA in pGex vector. Protein expression was induced by addition of isopropyl β-D–thiogalactoside (IPTG, 0.1 mM) at room temperature for 6 h.

Recombinant proteins (GST-Rab11a, GST-Rab5a, and GST-Rab7a) were purified (elution 10 mM glutathione, PBS), dialyzed, frozen in liquid nitrogen, and stocked (50% glycerol in Tris–HCl 50 mM 5 mM MgCl2, 100 mM NaCl) at −80 °C. His-Flag-tagged MTM1 was generated according to previously established protocol[25]. In brief, Flagged MTM1 was clone in vector and bacteria were grown in 2×-YT (16 g/L tryptone, 10 g/L yeast extract and 5 g/L NaCl) enriched medium until mid-log phase. Induction was performed with 1 mM IPTG at 16 °C for 12 h. Soluble protein fraction was purified, dyalized, and stocked (50% glycerol in 50 mM Tris–HCl 5 mM $MgCl_2$, 100 mM NaCl, 0.5% Triton).

Plasmids. The biosensor was built in sequential cloning steps using a monomeric version of fluorescent proteins (A206K mutation) to avoid signal artifacts during FRET quantitation caused by multimerization of biosensor molecules into limited diffusional space, such as in membrane and vesicular compartments. Rab11 binding domain (RBD11) was fused with RBD11-circularly permutated Venus (mcpVenus) at residue 195, and cyan fluorescent protein (mECFP)-Rab11a fusions were first constructed. Two repetitions of a linker encoding for a 17-mer unstructured soluble and proteinase-K sensitive polypeptide (GSTSGSGKPGSGEGSTK)[44] were then cloned by PCR to allow maximization of the FRET change between the active and inactive state. To construct RBD11-cpVenus, PCR was used to amplify amino acids 649–756 of FIP3 using the primers: 5′–CTAGCTAGCATGGGCCTGCAGGAGTACCACA–3′ and 5′–GCTCTAGAATGGGCACCCGCGACG–3′, and pGEX- FIP3 RBD11 as a template[9]. mcpVenus was amplified using the primers: 5′–GGTAGTGGTGAATTCATGCTCGGAGCAGTCCTGA–3′ and 5′–ATCCCCTCGAGAGCACGGGGCCGTCGCCGAT–3′ using ICUE3 FRET probe[45] as a template. Both fragments were then digested, gel purified, and subcloned in PGEM 3-T-Easy vector (Promega). The resulting fragment contained, from the 5′-end: a NheI site, RBD11, a EcoRI site, a linker (GGSG), and mcpVenus. This was cloned. To construct mECFP-Rab11a, a construct encoding mECFP was amplified with the following primers: 5′–AAGCGGCCGCATGGTGAGCAAGGGCGAGGAGCTG–3′ and 5′–GGTGCCCATTCTAGAAGTTCCCACGGGGGTACC-AGCCTTGTACAGCTCGT–3′. Rab11a was amplified with the following primers: 5′–GCTCTAGAATGGGCACCCGCGACG–3′ and 5′–GCGGATCCAATGCCTTAGATGTTCTGACAGCACTGC–3′ using a Rab11a expression construct as a template. Both fragments were then digested gel purified and subcloned in PGEM 3-T-Easy vector (Promega). The resulting fragment contained, from the 5′-end: a NotI site, a mECFP, a linker (GTPVGT), XbaI site, Rab11a and a BamHI site. In the next step, the 3′ end of RBD11-mcpVenus was flanked with zero, one or two copies of a sequence encoding a 17-mer peptide, (GSTSGSGKPGSGEGSTK) generated by PCR. For that purpose, seven annealed 5′ phosphorylated oligos, 5′–TCGAGGGGAGGCAGC–3′, 5′–GGCCGCTGC-CTCCCC–3′; 5′-TCGAGGGGATCAACTTCAGGATCAGGAAAACCCGGCTC-CGGCGAGGGATCAACTAAAAGC–3′;5′–GGCCGCTTTTAGTTGATCCCTC-GCCGGAGCCGGGTTTTCCTGATCCTGAAGTTGATCCCC–3′; 5′–TATATATATATATATACTCGAGGGATCAACTTCAGGATCAG-GAAAACCCGGCTCCGGCGAGGG–3′; 5′–CCGGGCTTGCCGCTGCCGGAA-GTAGAGCCTTTAGTTGATCCCTCGCCGGAGCCGGG–3′; and 5′–TATATATATATGCGGCCGCTTTTAGTTGATCCTTCTCCTGA-TCCGGGCTTGCCGCTGCCG-3′, that encode the linker sequence flanked at the 5′ by a XhoI and at the 3′ by a NotI restriction site were ligated and subcloned in PGEM 3-T-Easy vector (Promega). To assemble the biosensor all the subcloned fragments were digested with the single cutter enzyme inserted at the 5′ and 3′ends, gel purified and cloned in pcDNA3.1(-myc/His) vector (Invitrogen), thus originating the following fusion protein containing from the N terminus RBD11-cpVenu-2×17-mer linker-mECFP-Rab11a. The constructs were fully sequenced to ensure fidelity of the PCR reactions. Constitutively active (AS-$Rab11^{Q70L}$), dominant negative (AS-$Rab11^{S25N}$), a second constitutive active form (AS-$Rab11^{S20V}$), an RBD mutant (AS-$Rab11^{RBD\ mutant}$ in which the "RBD domain" of FIP3 carries a 3-amino-acid mutation abrogating binding of active Rab11)[31], a nucleotide free form (AS-$Rab11^{N124I}$) and a mutant lacking GDI interaction (AS-$Rab11^{N206X}$, in which Asn206 was changed to a stop codon, eliminating Rab11 prenylation/GDI binding site) versions of this biosensor were then engineered by site-directed mutagenesis (QuikChange kit, Stratagene) using the following primers: 5′-GATATGGGACACAGCAGGGCTAGAGCGATATCGAGC-3′; 5′-GCTCGATATCGCTCTAGCCCTGCTGTGTCCCATATC-3′; 5′-GATTCTGGTGTTGGAAAGAATAATCTCCTGTCTCG-3′; 5′-CGAGACAGGAGATTATTCTTTCCAACACCAGAATC-3′; 5′- GTTGTCCTTATTGGAGATGTTGGTGTTGGAAAGAGTA-3′; 5′- TACTCTTTCCAACACCAACATCTCCAATAAGGACAAC-3′; 5′-CAACTTCCGCCTGCAGGACGCCGCCGCCAGGATCATCGTGGCCATCAT-3′; 5′- ATGATGGCCACGATGATCCTGGCGGCGGCGTCCTGCAGGCGGAAGT TG-3′; 5′- GTTATCATGCTTGTGGGCATTAAGAGTGATCTACGTCATCTC-3′; 5′- GAGATGACGTAGATCACTCTTAATGCCCACAAGCATGATAAC-3′; 5′- ATGTTCCACCAACCACTGAATAAAAGCCAAAGGTGCAGTGCTG-3′; 5′- CAGCACTGCACCTTTGGCTTTTATTCAGTGGTTGGTGGAACAT-3′. Red fluorescent tagged versions of Rab5, Rab4, Rab11 and Rab7 were generated by PCR and cloned into the pmRFP-c1 plasmid.

The plasmid encoding RabGDI and GST-Rab7 were kindly provided by C. Bucci from University of Salento. To allow expression in mammalian cells the DNA sequence encoding RabGDI and flanked by EcoRI site at 5′ end and BamHI site at 3′-end was subcloned in pcDNA3.1(-myc/His) vector (Invitrogen). A FLAG tag (DYKDDDDK) was inserted by digestion of pcDNA3.1(-myc/His)-RabGDI with EcoRI followed by calf intestinal phosphatase (CIP) treatment and gel purification. The opened plasmid was ligated with a linker sequence encoding the FLAG epitope obtained by annealing two 5′ phosphorylated oligos with the following sequence: 5′–AATTCATGGACTACAAAGACGATGACGACAAGC-3′ and 5′–AATTGCTTGTCGTCATCGTCTTTGTAGTCCATG–3′. The plasmid encoding hSH3BP5 was kindly gifted by K. Sato from University of Gunma. A FLAG- N-terminal tag was added by PCR, and the product of this reaction was cloned in pcDNA3.1(-myc/His) vector, thus generating a FLAG-hSH3BP5. The plasmid encoding TBC1D9B was kindly provided by G. Apodaca from the University of Pittsburgh. A FLAG-N-terminal tag was added by PCR, and the product of this reaction was cloned in the pcDNA3.1(-myc/His) vector, thus generating a FLAG-TBC1D9B. The plasmid encoding mCherry-FYVE(2×) (pCI-neo-mCh-2XFYVE) was kindly gift by M. Bonazzi from University of Montpellier. The plasmid encoding TIAM1 was kindly gifted by G. Scita and A. Palamidessi from IFOM in Milan. The plasmid encoding Rabex-5 was kindly gifted by S. Sigismund from IFOM in Milan. The plasmid encoding RN-3 was kindly gifted by L. Lanzetti from IRCC in Candiolo.

Fluorometry assay. 2×10^5 HEK 293 T cells were plated in a 6-well plate and transfected using Lipofectamine 2000 (Invitrogen) according to the manufacturer's instructions. In experiments in which the biosensor was co-transfected with a negative or positive regulator, the biosensor/regulator DNA ratio was 1/4. The total amount of transfected DNA was kept to 500 ng. 36 h post-transfection, cells were lysed in lysis buffer (50 mM Tris–HCl, pH 7.4, 10 mM $MgCl_2$, 100 mM NaCl, 1% Triton X-100, proteinase inhibitors), and clarified lysate was placed in a fluorometer cuvette. The lysates were analyzed using a Fluoromax-4 Horiba fluorometer. The lysates were excited at 433 nm, and an emission scan was acquired from 450 to 550 nm. To normalize for biosensor concentration a second measurement was made by directly exciting YFP at 505 nm and measuring its emission at 525 nm.

Immunoprecipitation assay for interaction of AS-Rab11 with SH3BP5 or AS-Rab11 with TBC1D9B. HEK 293 T cells growing in 10-cm dishes were transfected with DNA mixtures containing 10 μg of pcDNA3.1(-myc/His)-Flag- SH3BP5 or 10 μg of pcDNA3.1(-myc/His)-AS-Rab11 or both, using calcium phosphate method. 48 h after transfection, cultures were harvested and homogenized in 0.5 ml lysis buffer (50 mM Tris–HCl, pH 7.4, 0.2 mM GDP, 10 mM $MgCl_2$, 100 mM NaCl, 1% Triton X-100, 50 mM sodium fluoride, 1 mM phenylmethylsulfonyl fluoride).

Cytosol was obtained by centrifuging the lysates at 20,000 *g* for 30 min at 4 °C, and protein concentration was determined by the Bradford method. 1 mg of cytosol was incubated with FLAG M2 antibody (SIGMA, St. Louis, Missouri, USA) or with 1 µg of anti-GFP antibody (Abcam, Cambridge, UK) for 2 h and incubated on a rotating rack for 1 h at 4 °C with Protein-G sepharose beads (GE, Buckinghamshire, UK). Samples were collected by centrifugation and washed six times with phosphate wash buffer (10 mM NaH_2Po_4, 137 mM NaCl, and 2.7 mM KCl). Bound FLAG-SH3BP5, FLAG-TBC1D9B or GFP-AS-Rab11 protein complexes were then eluted by adding Laemmli sample buffer. SDS–PAGE and western blotting followed standard procedures. A similar approach was employed for the RabGAP TBC1D9B using the following lysis buffer: 50 mM Tris–HCl, pH 7.4, 0.2 mM GTP, 10 mM $MgCl_2$, 100 mM NaCl, 1% Triton X-100, 50 mM sodium fluoride, 1 mM phenylmethylsulfonyl fluoride).

Immunoprecipitation assay for interaction of AS-Rab11 with GDI. HEK 293 T cells growing in 10-cm dishes were transfected with DNA mixtures containing 10 µg of pcDNA3.1(-myc/His)-Flag-RabGDI or 10 µg of pcDNA3.1(-myc/His)-AS-Rab11 or both, using the calcium phosphate method. 48 h after transfection, cultures were harvested and gently homogenized in 0.5 ml of lysis buffer (50 mM Tris–HCl, pH 7.4, 0.2 mM GDP, 10 mM $MgCl_2$, 50 mM sodium fluoride, and 1 mM phenylmethylsulfonyl fluoride). Cytosol was obtained by centrifuging the lysates at 20,000 *g* for 30 min at 4 °C, and protein concentration was determined by Bradford method. 1 mg of cytosol was incubated with FLAG M2 antibody (SIGMA, St. Louis, Missouri, USA) or with 1 µg of anti-GFP antibody (Abcam, Cambridge, UK) for 2 h and incubated on a rotating rack for 1 h at 4 °C with Protein-G sepharose beads (GE, Buckinghamshire, UK). Samples were collected by centrifugation and washed six times with phosphate wash buffer (10 mM NaH_2Po_4, 137 mM NaCl, and 2.7 mM KCl). Bound FLAG-GDI or GFP-AS-Rab11 protein complexes were then eluted by adding Laemmli sample buffer. SDS–PAGE and western blotting followed standard procedures.

Radiolabeling of intracellular nucleotides and identification of the nucleotide-bound forms of AS-Rab11. HEK293T cells cultured in 6-well plate dishes and transfected for 48 h were radiolabeled for 4 h with ^{32}P (6.0 MBq per dish) in phosphate-free DMEM (Invitrogen, Cat. Number 11971025). The expression levels of AS-Rab11 proteins and mutant forms were assessed by immunoblot analysis with the anti-GFP antibody (Abcam, Cambridge, UK). The labeled cells (7×10^5 cells) were lysed with 0.3 ml of an ice-cold solubilizing buffer consisting of 40 mM Tris–HCl (pH 7.5), 100 mM NaCl, 20 mM $MgCl_2$, 1 mM Na_3VO_4, 1 mM dithiothreitol, 1% (w/v) Triton X-100, and 2 µg/ml aprotinin and clarified. The precleared lysates were incubated with anti-GFP antibody–immobilized Protein G–Sepharose beads (GE Healthcare) at 4 C for 30 min. After extensive washing of the immunocomplexes, associated nucleotides were separated by thin-layer chromatography and quantified with a Amersham Hyperfilm MP (GE Healthcare).

Guanine nucleotide exchange assay. HEK 293 T cells growing in 10-cm dishes were transfected with DNA mixtures containing 10 µg of pEGFP-Rab11a or 10 µg of pcDNA3.1(-myc/His)-AS-Rab11, using a calcium phosphate method. At 48 h after transfection, cultures were harvested and homogenized in 1 ml of lysis buffer (50 mM HEPES, pH 7.6, and 1% (v/v) Triton-X-100, 100 mM NaCl, protease inhibitors). Cytosol was obtained by centrifuging the lysates at 20,000*g* for 20 min at 4 °C, and protein concentration of clarified lysates was determined by the Bradford method. 1 mg of protein was immunoprecipitated using 1 µg of anti-GFP antibody (Abcam, Cambridge, UK) for 1 h and incubated on a rotating rack for 1 h at 4 °C with Protein-G sepharose beads (GE, Buckinghamshire, UK). Samples were collected by centrifugation and washed six times with buffer A containing 50 mM HEPES, pH 7.6, 1 mM DTT and 20 mM EDTA and incubated for 20 min at 25 °C to remove Mg^{2+} and nucleotide bound to the Rab11 GTPases. The treatments of the samples with buffer A were repeated three times more. To determine the GDP binding affinities to Rab11 GTPases, [3 H]GDP at a specific activity of 6,000 c.p.m./µM was incubated with the respective apo-GTPases at 25 °C for 1 h in buffer B, containing 50 mM HEPES, pH 7.6, 100 mM NaCl, 2.5 mM $MgCl_2$ and 1 mM DTT. Samples were collected by centrifugation and washed six times with buffer C, containing 50 mM HEPES, pH 7.6, 100 mM NaCl, 10 mM $MgCl_2$ to stop the binding reaction, and the radionucleotides remaining bound to the Rab GTPases were quantified by scintillation counting. To measure the GDP/GTP exchange from Rab11 GTPases, the immunoprecipitated apo-GTPases were first complexed with [3 H]GDP or in buffer B. After 60 min a binding equilibrium was reached, the dissociation reactions were initiated by the addition of 500 µM GTPγS to the incubation mixtures. At the indicated time intervals, samples were collected by centrifugation and washed six times with buffer C to stop the exchange reaction. The radionucleotides remaining bound to the Rab GTPases were quantified by scintillation counting.

Rab11-activity pull down assay. Cells were washed in ice-cold PBS and lysed in 1 ml of MLB buffer (25 mM HEPES (pH 7.5), 150 mM NaCl, 1% Igepal CA-630, 10% glycerol, 25 mM NAF, 10 mM $MgCl_2$, 1 mM EDTA, 1 mM sodium orthovanadate, and protease inhibitor cocktail). Supernatant was collected after 15 min centrifugation at 13,000 r.p.m. A total of 1 mg of protein extract was incubated with 30 µg of recombinant protein coupled with glutathione *S*-transferase agarose (GE, Buckinghamshire, UK). The reaction mixture was gently rocked for 1 h at 4 °C. Beads were washed four times with lysis buffer. Samples were resuspended in Laemmli buffer for SDS–PAGE and immunoblot analysis. Endogenous content of total Rab11 in cell lysates was measured by loading 50 µg of total extracts in a different gel followed by immunoblot and used to normalize measurements of active Rab11. For quantification analysis, pictures were taken ensuring that intensity was within the linear range and the Quantity One 1-D analysis software (Bio-Rad) was used.

Rab11-effectors pull-down assay. 50 µg of GST-Rab11 and a corresponding molar amount of GST recombinant proteins were coupled to with glutathione *S*-transferase agarose (GE, Buckinghamshire, UK) and gently rocked for 1 h at 4 °C. Samples were collected by centrifugation and washed six times with buffer A containing 50 mM HEPES, pH 7.6, 1 mM DTT and 20 mM EDTA and incubated for 20 min at 25 °C to remove Mg^{2+} and nucleotide bound to the Rab11 GTPases. The treatments of the samples with buffer A were repeated three more times. GDP or GTPγS was added at a final concentration of 2 mM and incubated with the respective apo-GTPases at 25 °C for 1 h in buffer B containing 50 mM HEPES, pH 7.6, 100 mM NaCl, 2.5 mM $MgCl_2$ and 1 mM DTT. Samples were collected by centrifugation and washed six times with buffer C containing 50 mM HEPES, pH 7.6, 100 mM NaCl, 10 mM $MgCl_2$ to stop the binding reaction. Proteins on beads were incubated with either 1 ml of cell lysate made from a confluent dish of COS-7 cells lysed in 1 ml of MLB buffer (25 mM HEPES (pH 7.5), 150 mM NaCl, 1% Igepal CA-630, 10% glycerol, 25 mM NAF, 10 mM $MgCl_2$, 1 mM EDTA, 1 mM sodium orthovanadate, and protease inhibitor cocktail) or with recombinant purified protein diluted in GST-binding buffer (20 mM Tris–HCl (pH 7.4), 100 mM NaCl, 5 mM MgCl2, 0.5% Triton X-100, 5 mg/ml BSA). After 1 h, beads were washed with MLB or GST-binding buffer and proteins solubilized by boiling in LDS sample buffer.

Transferrin recycling assay. 2×10^5 COS-7 cells were plated in a 6-well plate. After 24 h, cells were starved for 2 h in serum-free DMEM containing 0.1% BSA at 37 °C, 5% CO_2 and then, where required, pretreated with 0.1% DMSO as control or with Vps34-IN1 1 µM for 30 min. 20 µg/ml of Alexa Fluor 647- conjugated human transferrin (Invitrogen) were added for 30 min. After 37 °C PBS washing, DMEM containing 0.1% BSA at 37 °C, 5% CO_2 was added at various length times. Cells were then washed twice with cold PBS, and acid stripping solution (150 mM NaCl, 2 mM $CaCl_2$ and 25 mM CH_3COONa, pH 4.5) was added for 4 min. For FACS analysis, cells were detached with PBS containing 0.5 mM EDTA and fixed in 4% paraformaldehyde for 10 min. After resuspension in PBS, fluorescence flow cytometry was performed using a FACScalibur instrument. 20,000 cells were collected for each sample. The MFI of the cell population was recorded for each time point. Data were normalized to the time 0 MFI. For immunofluorescence analysis, cells were fixed in 4% paraformaldehyde for 10 min and imaged by confocal microscopy.

Internal transferrin quantitation. 2×10^5 COS-7 wild-type (or interfered) cells were plated in a 6-well plate. After 24 h, cells were starved for 2 h in serum-free DMEM containing 0.1% BSA at 37 °C, 5% CO_2, and then, where required, pretreated with 0.001% DMSO as control or with Vps34-IN1 1 µM for 30 min. 20 µg/ml of Alexa Fluor 647-conjugated human transferrin (Invitrogen) was added for 30 min to allow continuous uptake and recycling of labeled ligands. Cells were then washed twice with cold PBS and acid stripping solution (150 mM NaCl, 2 mM $CaCl_2$ and 25 mM CH_3COONa, pH 4.5) was added for 4 min. Cells were detached with PBS 0.5 mM EDTA and fixed in 4% paraformaldehyde for 10 min. After resuspension in PBS, fluorescence flow cytometry was performed using a FACScalibur instrument. 20,000 cells were collected for each sample. The MFI of the cell population was recorded for each time point. Data were normalized to control MFI values. For immunofluorescence analysis, cells were fixed in 4% paraformaldehyde for 10 min and imaged by confocal microscopy.

Cell imaging. Cells were grown on µ-Dish 35 mm, high-imaging dishes (Ibidi). Imaging was performed in CO_2 independent medium, Dulbecco's modified Eagle's medium without FBS (GIBCO). Time-lapse series were acquired at 37 °C on an inverted confocal Leica SP8 microscope with AOBS equipped with 40× O2/Oil immersion objective, NA 1.30. The temperature was controlled by a climate box covering the set up. Hyd detectors (Leica) allowed the simultaneous detection of mECFP and mcpVenus or/and mCherry/mRFP, respectively. Fluorescent dyes were imaged sequentially in frame-interlace mode to eliminate cross-talk between the channels. mECFP was excited with a 458-nm laser line and imaged at 470–500-nm bandpass emission filters. mcpVenus was exited with the 514-nm argon laser line and imaged through a 525–550-nm bandpass emission filter. mCherry/mRFP was excited with the 568-nm helium neon laser line and imaged through a 580–650-nm bandpass emission filter. Alexa 647 dye was excited with the 633 nm helium neon laser line and imaged through a 650–700-nm bandpass emission filter. Serial sections were acquired satisfying the Nyquist criteria for sampling and processed using Matlab (MathWorks, MA, USA) and ICY software (http://icy.bioimageanalysis.org). Signals were referred to as individual structures if they

comprised of a continuous patch of intensity values 50 (in a range of 0–255). At least two sections per cell were counted, ensuring that peripheral and perinuclear structures were equally taken into account. mECFP was bleached 5–10 times (2 s/scan) with zoom (×15) with 100% laser power of the 458 nm Argon laser line. At the beginning of each experiment, the number of bleaching steps that were sufficient to bleach mECFP was assessed and was kept constant all through. Acquisition was performed at zoom (×11) in a region of 26 µm inside. The ROI has been chosen to contain the photobleached ERC and the surrounding intracellular region, and over a region sufficiently large and homogeneous to be able to visualize vesicles moving toward it. Exposure times and readout were fixed as follows: 200–300 ms for each channel followed by a 60-ms readout delay for the experiment in Fig. 3a–f, I and 4b–g), resulting in time-lapse sequences of roughly one frames per second. The time lapse sequences of roughly one frame per 30 s was used in Fig. 3g,h and Supplementary Figs. 4a and 5a,b,d. Images obtained were merged and exported as a single TIFF file.

Image/video processing and data analysis. Image processing and analysis for total FRET activation in the cell were carried out with the Matlab software (MathWorks, MA, USA) integrated with Image Processing and Bio-formats Toolbox. Following Gaussian smoothing, the image was converted to binary through thresholding, then median filtering, morphological closing and holes filling were applied to eliminate noisy pixels and smooth the images. The final mask was obtained by computing the distance transform of the binary image and using it as the input for a watershed transform, thus enabling discrimination and separation of different contiguous endosomes from one to another. The threshold mask was then applied to sensitized FRET and CFP images, and background subtraction was performed according to a previously published protocol[46]. Finally, FRET activity ratio was calculated by dividing the unsaturated sensitized FRET pixels by the CFP pixels[47,48]. To measure the dependence of FRET ratio on the distance from the nucleus, endosomes present in each frame included in the threshold mask were binned according to the distance of their centroid from the nuclear membrane.

Video processing and analysis for particle tracking and vesicle intensity profile were carried out with ImageJ, ICY[49] and R studio. Following background subtraction and Gaussian smoothing the CFP, FRET sensitized, YFP and red fluorescence were treated to eliminate noisy pixels and smooth the images. The FRET ratio for each frame was computed by dividing FRET sensitized signal by CFP signal. The videos were then imported in ICY for spot detection and particle tracking procedure performed on the YFP signal[50]. Intensity profiles for FRET ratio, YFP and FYVE2X were exported together with the trajectory for each detected vesicle. Vesicle intensity profiles were then aligned in R studio according to their speed profile and direction. The vesicle mean FRET ratio was adjusted by substracting cytoplasmic mean FRET ratio.

MatLab code is fully available on GitHub.

Statistical analysis. For biochemical, immunocytochemistry and microscopy-based experiments, a minimum of three independent experiments (n) were performed and statistically significant estimates for each sample were obtained. For microscopy-based quantification, cells were chosen arbitrarily according to the fluorescence signal in a separate channel, which was not used for quantification when possible. Values were presented as means ± s.e.m. P values were calculated using two-tailed Student's t test and one- or two-way ANOVA followed by Bonferroni's multiple comparison posttest (GraphPad Software). Statistical significance is indicated as follows: $^{*}P<0.05$; $^{**}P<0.01$; and $^{***}P<0.005$.

Reporting Summary. Further information on experimental design is available in the Nature Research Reporting Summary linked to this article.

Data availability. The data that support the findings of this study are available from the corresponding authors upon reasonable request.

References

44. Whitlow, M. et al. An improved linker for single-chain Fv with reduced aggregation and enhanced proteolytic stability. *Protein Eng.* **6**, 989–995 (1993).
45. DiPilato, L. M. & Zhang, J. The role of membrane microdomains in shaping β2-adrenergic receptor-mediated cAMP dynamics. *Mol. Biosyst.* **5**, 832–837 (2009).
46. Broussard, J. A., Rappaz, B., Webb, D. J. & Brown, C. M. Fluorescence resonance energy transfer microscopy as demonstrated by measuring the activation of the serine/threonine kinase Akt. *Nat. Protoc.* **8**, 265–281 (2013).
47. Kardash, E., Bandemer, J. & Raz, E. Imaging protein activity in live embryos using fluorescence resonance energy transfer biosensors. *Nat. Protoc.* **6**, 1835–1846 (2011).
48. Jares-Erijman, E. A. & Jovin, T. M. FRET imaging. *Nat. Biotechnol.* **21**, 1387–1395 (2003).
49. de Chaumont, F. et al. Icy: an open bioimage informatics platform for extended reproducible research. *Nat. Methods* **9**, 690–696 (2012).
50. Chenouard, N., Bloch, I. & Olivo-Marin, J. C. Multiple hypothesis tracking for cluttered biological image sequences. *IEEE Trans. Pattern Anal. Mach. Intell.* **35**, 2736–3750 (2013).

nature research

Corresponding author(s): Emilio HIrsch, Carlo Cosimo Campa

Reporting Summary

Nature Research wishes to improve the reproducibility of the work that we publish. This form provides structure for consistency and transparency in reporting. For further information on Nature Research policies, see Authors & Referees and the Editorial Policy Checklist.

Statistical parameters

When statistical analyses are reported, confirm that the following items are present in the relevant location (e.g. figure legend, table legend, main text, or Methods section).

n/a	Confirmed	
☐	☒	The exact sample size (*n*) for each experimental group/condition, given as a discrete number and unit of measurement
☐	☒	An indication of whether measurements were taken from distinct samples or whether the same sample was measured repeatedly
☐	☒	The statistical test(s) used AND whether they are one- or two-sided *Only common tests should be described solely by name; describe more complex techniques in the Methods section.*
☐	☒	A description of all covariates tested
☐	☒	A description of any assumptions or corrections, such as tests of normality and adjustment for multiple comparisons
☐	☒	A full description of the statistics including central tendency (e.g. means) or other basic estimates (e.g. regression coefficient) AND variation (e.g. standard deviation) or associated estimates of uncertainty (e.g. confidence intervals)
☐	☒	For null hypothesis testing, the test statistic (e.g. *F*, *t*, *r*) with confidence intervals, effect sizes, degrees of freedom and *P* value noted *Give P values as exact values whenever suitable.*
☒	☐	For Bayesian analysis, information on the choice of priors and Markov chain Monte Carlo settings
☒	☐	For hierarchical and complex designs, identification of the appropriate level for tests and full reporting of outcomes
☐	☒	Estimates of effect sizes (e.g. Cohen's *d*, Pearson's *r*), indicating how they were calculated
☐	☒	Clearly defined error bars *State explicitly what error bars represent (e.g. SD, SE, CI)*

Our web collection on statistics for biologists may be useful.

Software and code

Policy information about availability of computer code

Data collection	Cellquest, Las X
Data analysis	Excel, cell quest, Mathlab R2015a, Icy1.9.4.0, Quantity One 1D, ImageJ 1.51t 31 , R studio v1.1.442, GraphPad PRISM 7.0, Fiji 2015v

For manuscripts utilizing custom algorithms or software that are central to the research but not yet described in published literature, software must be made available to editors/reviewers upon request. We strongly encourage code deposition in a community repository (e.g. GitHub). See the Nature Research guidelines for submitting code & software for further information.

Data

Policy information about availability of data

All manuscripts must include a data availability statement. This statement should provide the following information, where applicable:

- Accession codes, unique identifiers, or web links for publicly available datasets
- A list of figures that have associated raw data
- A description of any restrictions on data availability

Biochemichal data and imaging data are available upon request.

Field-specific reporting

Please select the best fit for your research. If you are not sure, read the appropriate sections before making your selection.

☒ Life sciences ☐ Behavioural & social sciences ☐ Ecological, evolutionary & environmental sciences

For a reference copy of the document with all sections, see nature.com/authors/policies/ReportingSummary-flat.pdf

Life sciences study design

All studies must disclose on these points even when the disclosure is negative.

Sample size	For imaging data and quantitation of a minumum of 3 biological replicates were quantified (50 distinct pictures). For biochemichal data and quantitation of a minumum of 3 biological replicates were quantified. For FACS data a minimum of 3 biological replicates were quantified.
Data exclusions	Data were excluded if either positive controls were found negative or if negative controls were found positive.
Replication	Each experiment was designed to include positive and negative controls choose to be in line with previously published literature. Experiments were performed a minumum of 3 times and only those that satisfy positive and negative controls were analyzed.
Randomization	Random selection of sample from the population was performed
Blinding	Blinding was performed by measuring signal in a different channel.

Reporting for specific materials, systems and methods

Materials & experimental systems

n/a	Involved in the study
☐	☒ Unique biological materials
☐	☒ Antibodies
☐	☒ Eukaryotic cell lines
☒	☐ Palaeontology
☒	☐ Animals and other organisms
☒	☐ Human research participants

Methods

n/a	Involved in the study
☒	☐ ChIP-seq
☐	☒ Flow cytometry
☒	☐ MRI-based neuroimaging

Unique biological materials

Policy information about availability of materials

Obtaining unique materials	Unique Material used are available from author.

Antibodies

Antibodies used	The following antibodies were used in this study: mouse-anti-PI3K-C2α (BD Biosciences 611046, western blotting (WB) 1:500), mouse-anti-Rab11 (BD Biosciences 610656, WB 1:1000), rabbit-anti-MTM1 (SIGMA HPA010008, WB 1:1000), mouse-anti-FLAG (SIGMA clone M2, WB 1:2000), mouse-anti-GFP (ABCAM ab127417, WB 1:1000), rabbit-anti-VPS34 (Novus Biologicals NB110-87320SS, WB 1:1000), mouse-anti-MTMR4 (Santa Cruz sc-373922, WB 1:500), mouse-anti-MTMR6 (ABCAM ab69875, WB 1:1000), mouse-anti-MTMR9 (Santa Cruz sc-514366, WB 1:1000), rabbit-anti-FIP2 (ABCAM ab76892, WB 1:1000), rabbit-anti-FIP4 (Biorbyt orb215321, WB 1:1000). Anti-mouse IgG (ab131368) Anti-Rabbit IgG (A0545 SIGMA). anti mouse/rabbit IgG Alexa fluor 488/568.
Validation	anti-PI3K-C2α and anti-Rab11 validated (Franco I, et al.; Dev Cell; 2014). anti-MTM1 validated (Agrawal PB, et al.; Am J Hum Genet. 2014). anti-FLAG (more than 300 publication see provider list). anti-GFP validated (Bae EJ et al.; Nat Commun.; 2014). anti-VPS34 (Shi JM.; Biochem Pharmacol.; 2013).

Eukaryotic cell lines

Policy information about cell lines

Cell line source(s)	ATCC
Authentication	cell were not autenticated
Mycoplasma contamination	Cells were negative for Mycoplasma and routinely tested.
Commonly misidentified lines (See ICLAC register)	No commonly misidentified cell lines were used

Flow Cytometry

Plots

Confirm that:

☒ The axis labels state the marker and fluorochrome used (e.g. CD4-FITC).

☒ The axis scales are clearly visible. Include numbers along axes only for bottom left plot of group (a 'group' is an analysis of identical markers).

☒ All plots are contour plots with outliers or pseudocolor plots.

☒ A numerical value for number of cells or percentage (with statistics) is provided.

Methodology

Sample preparation	Cells were detached with PBS 0.5 mM EDTA and fixed in 4% paraformaldehyde for 10 min. Procedures were listed in material and method section
Instrument	FACScalibur
Software	Cellquest
Cell population abundance	100%
Gating strategy	cell debris were removed by FSC/SSC gating strategy. gating on GFP expressing cells was performed.

☒ Tick this box to confirm that a figure exemplifying the gating strategy is provided in the Supplementary Information.